Article

Carbon dioxide sink in the Arctic Ocean from cross-shelf transport of dense Barents Sea water

Andreas Rogge [1,2] ✉, Markus Janout [2], Nadezhda Loginova [3], Emilia Trudnowska [4], Cora Hörstmann [2,5], Claudia Wekerle [2], Laurent Oziel [2], Vibe Schourup-Kristensen [6], Eugenio Ruiz-Castillo[2], Kirstin Schulz [7], Vasily V. Povazhnyy[3], Morten H. Iversen [2,8] & Anya M. Waite[2,9,10]

Large amounts of atmospheric carbon can be exported and retained in the deep sea on millennial time scales, buffering global warming. However, while the Barents Sea is one of the most biologically productive areas of the Arctic Ocean, carbon retention times were thought to be short. Here we present observations, complemented by numerical model simulations, that revealed a deep and widespread lateral injection of approximately 2.33 kt C d^{-1} from the Barents Sea shelf to some 1,200 m of the Nansen Basin, driven by Barents Sea Bottom Water transport. With increasing distance from the outflow region, the plume expanded and penetrated into even deeper waters and the sediment. The seasonally fluctuating but continuous injection increases the carbon sequestration of the Barents Sea by 1/3 and feeds the deep sea community of the Nansen Basin. Our findings combined with those from other outflow regions of carbon-rich polar dense waters highlight the importance of lateral injection as a global carbon sink. Resolving uncertainties around negative feedbacks of global warming due to sea ice decline will necessitate observation of changes in bottom water formation and biological productivity at a resolution high enough to quantify future deep carbon injection.

Without the buffering function of the world oceans, the impact of anthropogenic greenhouse gas emissions would be far more dramatic[1]. The retention time of up to 25% of human CO_2 emissions from the atmosphere[2,3] strongly depends on the local export efficiency and sequestration depth. Photosynthetically fixed particulate organic

carbon (POC) can increase retention times drastically due to gravitational sinking into deeper waters or sediments isolating it from the atmosphere for long time scales[4]. POC fluxes are traditionally considered to decrease exponentially with depth due to ongoing grazing and respiration[5]. However, a major uncertainty in such vertical
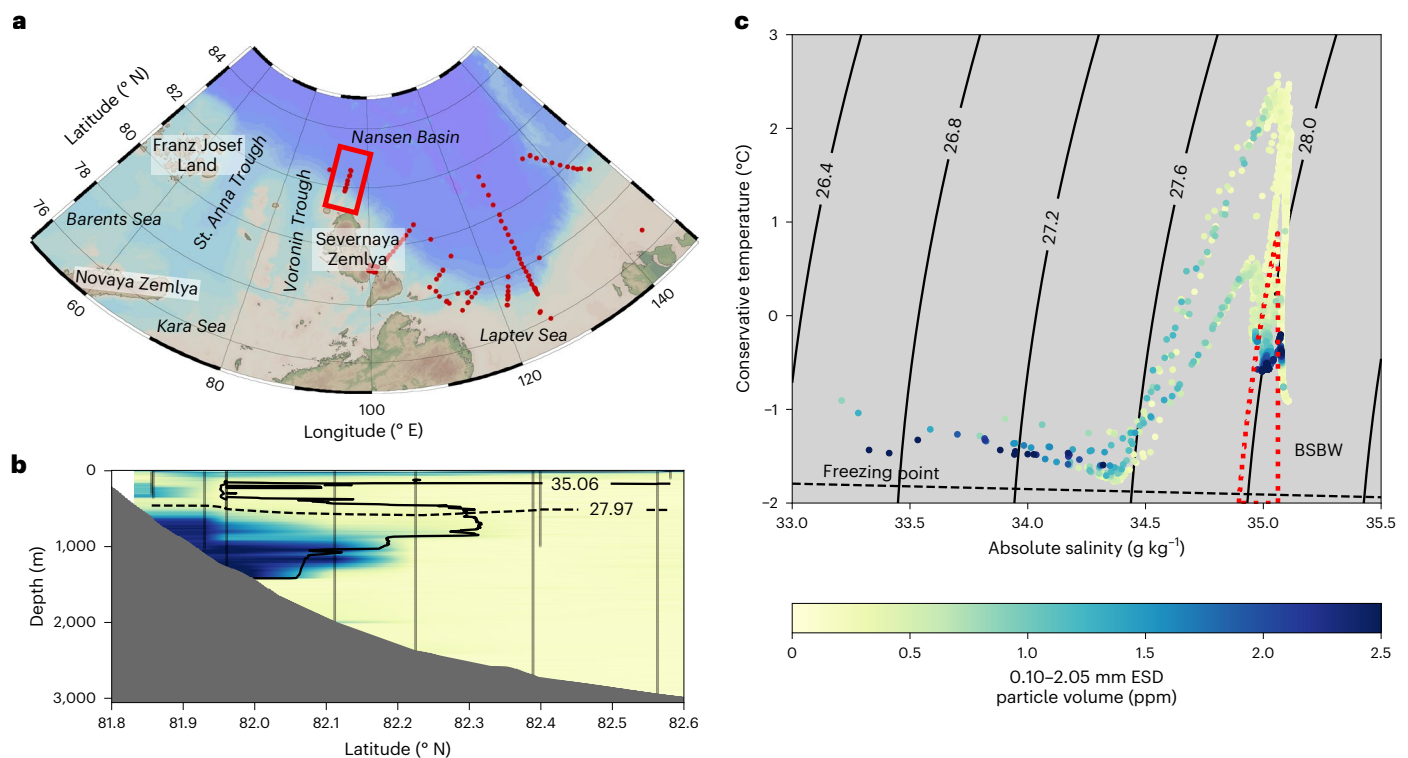
Fig. 1 | Deep particle plume and its relation to BSBW north of Severnaya Zemlya. a, Map of the research area including CTD stations (red dots) with the shown transect closest to the outflow area (red rectangle). **b**, Spatial particle volume distribution of the size fraction 0.1–2 mm measured along the transect. The area above the solid (absolute salinity <35.06 g kg⁻¹) and below the dashed isoline (potential density anomaly >27.97 kg m⁻³) indicates BSBW. **c**, Conservative temperature and absolute salinity plot with different colours showing particle volume of the size fraction 0.1–2 mm and relation of particle maximum with BSBW. Isolines indicate potential density anomaly (σ0) in kg m⁻³. BSBW is located within red dashed water mass polygon. Particle volumes have the same colour bar in **b** and **c**.

decay models is lateral transport, which, if substantial, would cause an increased input of POC at depth and decouple sources and sinks. These processes are rarely studied and generally not considered in global biogeochemical models. In the Amerasian basin of the Arctic Ocean, eddy transport[6] and advection of benthic nepheloid layers[7,8] have been identified as lateral transport processes to moderate depths, which might also partly explain a reported mismatch between local primary production and benthic carbon demand in the Arctic deep sea[9]. In the Eurasian basin, however, comparable studies are missing, although dense bottom waters, produced on the Russian shelf[10,11], have the potential to inject an important carbon signature directly into the deep sea due to density-driven subduction. Notably, the Barents Sea is a hotspot of dense water formation[12,13] but also CO_2 uptake and fixation. With 36.4 Mt C yr⁻¹, it contributes ~20% of the pan-Arctic CO_2 uptake (180 Mt C yr⁻¹) (ref. [14]) and with 102 Mt C yr⁻¹ (ref. [15]), ~50 % of the total primary production[16], but due to the lack of data from the dense water outflow region, its impact on the Arctic carbon budget is still not resolved. Here we present results of the campaign ARCTIC2018 onboard RV Akademik Tryoshnikov in the Nansen Basin and the Laptev Sea. Combining underwater imaging with water mass and circulation measurements, molecular sequencing techniques and model calculations, we show that dense water-driven carbon injection may provide an important pathway for Arctic carbon sequestration.

Bottom water-associated lateral particle transport

In late summer 2018, we performed transects of vertical profiles within the Nansen Basin east of St. Anna Trough (Fig. 1a) using a conductivity, temperature and depth sensor (CTD) equipped with a fluoro- and turbidimeter and an Underwater Vision Profiler 5hd

(UVP)[17] camera system to measure particle size distribution and abundance. Our data showed a widespread plume of particles in the Nansen Basin, which was most pronounced north of Severnaya Zemlya (Fig. 1), where the maximum volume of particles 0.102–2.05 mm equivalent spherical diameter (ESD; further particles 0.1–2 mm) reached 3.5 mm³ l⁻¹ (ppm). This plume extended over a cross section of 19.5 km² between 500 m and 1,200 m and more than 40 km off the shelf and was co-located with Barents Sea Bottom Water (BSBW) characterized by absolute salinities <35.06 g kg⁻¹ and potential density anomalies >27.97 kg m⁻³ (Fig. 1c).

BSBW is formed by the transformation of North Atlantic waters during its passage through the Barents Sea due to cooling and mixing with shelf waters and brine, rejected during sea ice formation[10,13]. Water mass definition was based on this transformation: after leaving the shelf system BSBW north of Severnaya Zemlya was denser than waters in the intermediate density layer and less saline than dense Atlantic water from Fram Strait (Methods).

After leaving the shelf through St. Anna Trough, BSBW integrates into the respective density horizon below the Atlantic core of the Arctic Boundary Current. Steered by the Coriolis force, it propagates along the shelf break further east towards our study area[11,12]. The particle concentrations were low in depths shallower than 500 m, typical for Atlantic water in this region (Fig. 1b). Increased concentrations of particles below were hence transported laterally with the advection of BSBW. The presence of particles >0.1 mm, mainly in deeper layers of BSBW or below (Fig. 1b, Extended Data Fig. 1b–d) indicated gravitational sinking, resulting in a spatial separation during water mass propagation from the outflow region located several tens of km upstream. Increased turbidity exhibited a higher co-location with BSBW signals (Fig. 2), pointing to a high load of small particles in suspension within this water
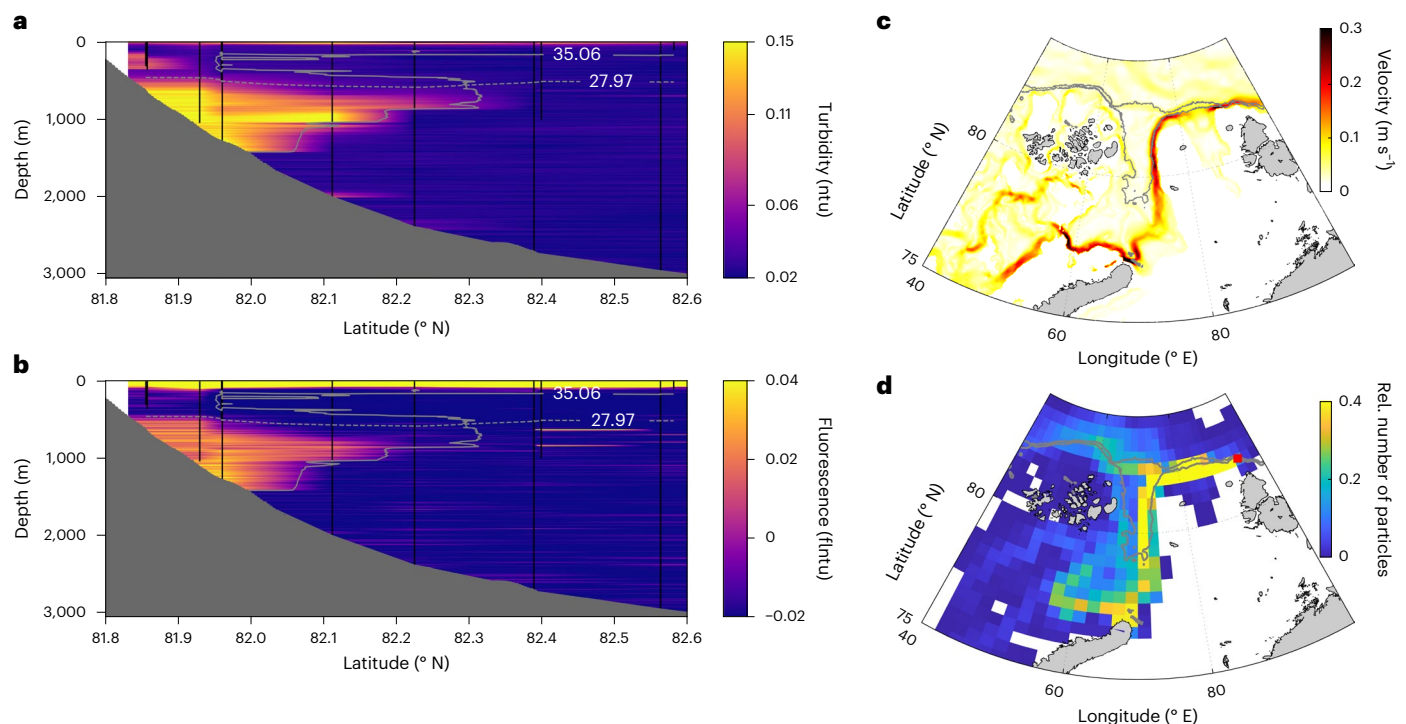
Fig. 2 | Increased turbidity and fluorescence signals within BSBW in the transect north of Severnaya Zemlya and modelled origin of the material. **a,b**, Spatial distribution of turbidity (**a**) and fluorescence (**b**) measured along the transect. The areas above the solid (absolute salinity <35.06 g kg⁻¹) and below the dashed isolines (potential density anomaly >27.97 kg m⁻³) indicate BSBW. **c**, Mean ocean current velocity at 200 m depth simulated by the Finite-Element Sea ice-Ocean Model (FESOM) visualizes the main current field of the Barents Sea branch

of the Arctic Boundary Current. **d**, FESOM-based backward trajectories shown as relative number of particles 0.08 mm ESD (sinking velocity of 1.03 m d⁻¹) as representative particle class for the non-ballasted small suspended particle size fraction <0.1 mm indicate a shelf-based origin of large fractions of the particle load even from the northern Barents Sea. Red square in **d** indicates the particle endpoint in the observed plume.

mass. Especially this material, characterized by low sinking velocities, has the potential for long-range transport.

Origin and evolution of the particle plume

To identify the origin of the material observed within the plume, we performed particle backtracking calculations using the Finite-Element Sea ice-Ocean Model (FESOM[18]; Extended Data Fig. 2a–c), which confirmed a lateral injection from the shelf (Fig. 2c,d and Extended Data Fig. 2d–g). Reverse trajectories showed that large fractions of particles originated in the St. Anna Trough region on the shelf following the main ocean current field into the basin. More than half of the non-ballasted particle fraction <0.1 mm originated ~750 km upstream within the northeastern Barents Sea close to Novaya Zemlya (Extended Data Table 1). Open waters of lee polynyas with increased sea ice formation rates in this area are a known hotspot of BSBW formation[12,13]. Furthermore, enhanced primary productivity compared with the Arctic basin due to increased light availability within the marginal ice zone and polynyas in combination with nutrients from Atlantic waters, freshwater run-off and wind-induced vertical mixing[19–21] is characteristic for this region. On the other hand, deep mixing together with enhanced aggregation leads to high export efficiencies[22–25], whereas strong mean and tidal currents keep the material in suspension in the frictional bottom boundary layer, which prevents burial in the sediment[26] and promotes resuspension.

The FESOM simulations included a warm bias of ~1 °C, leading to an underestimation of BSBW production and therefore also of the shelf-originating particle load. However, several lines of field evidence support the non-local origin of the particles: (1) 16S and 18S rRNA gene amplicon sequencing revealed that the microbial community of the suspended particle fraction <0.1 mm differed significantly in the plume

(*P* < 0.01; Extended Data Fig. 3). Moreover, (2) we identified the benthic indicator species *Dolichomastigaceae*, recently isolated from deep sea sediments[27], to be associated with those particles (Supplementary Table 1). (3) Increased fluorescence signals in the plume (Fig. 2b) point towards a phytoplanktonic origin of fractions of the particle load. (4) The majority of marine snow >0.8 mm within the plume consisted of degraded phytodetritus aggregates as identified in UVP images (Extended Data Fig. 1). Their distinct circular and compact morphology has been described as characteristic for processed aggregates during ending Arctic phytoplankton blooms[28]. (5) Abundances of copepods >0.8 mm were increased within the plume (Extended Data Fig. 1g). UVP images showed intact and healthy-looking copepods, suggesting they were alive and probably actively grazing. Synthesizing this list of field evidence with our model results above, the particle load transported with BSBW can be described as a mixture of fresh material from the phytoplankton-grazer community within the euphotic shelf zone and resuspended material from sediments.

As a result of this mixed pool of non-local relatively fresh and old material, also particulate C:N ratios revealed contradictory results: low C:N ratios of particles <0.1 mm are typical for cold, nutrient-rich, high-latitude waters[29], possibly promoted by diatoms[30] and heterotrophic eukaryotes[31] as identified within our amplicon sequences (Supplementary Table 1). Particles >0.1 mm, on the other hand, showed C:N ratios up to >40 (Extended Data Fig. 4), especially within the transect closest to the BSBW outflow region. Because surface samples—but not the fraction <0.1 mm—also were affected, we suggest extrapolymeric substances, such as polysaccharides within large phytoaggregates[32], to have caused these values. These substances are carbon-rich, nitrogen-poor and buoyant, which might also support long-range lateral transport due to reduced sinking velocities.
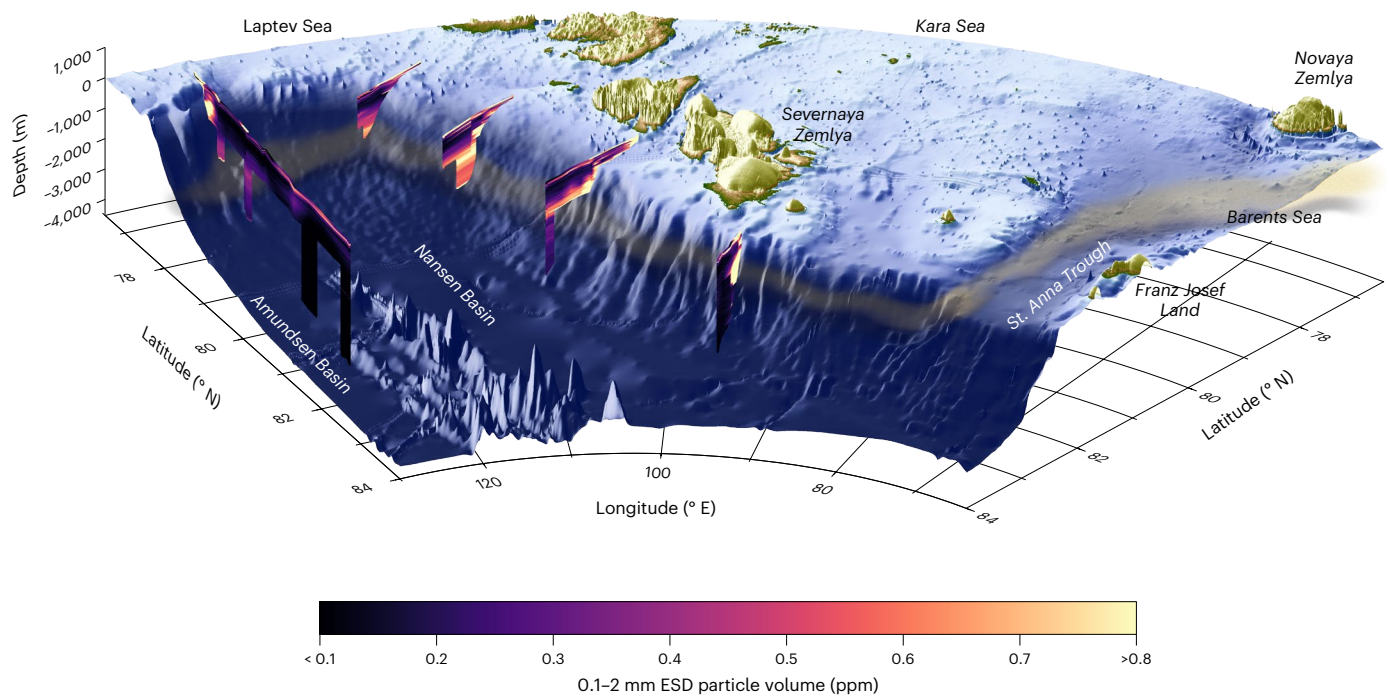
Fig. 3 | Spatial particle distribution >0.1 mm in transects of the Nansen and Amundsen basins. Golden shade illustrates the path of particle-loaded BSBW from the Barents Sea shelf through St. Anna Trough and along the continental slope of the Eurasian Basin towards the observed plume.

In the course of the campaign, we could follow the path of BSBW and its particle load further along the shelf break. Approximately 250 km downstream the first observation, east of Severnaya Zemlya (Extended Data Fig. 5b,c), the plume reached twice as far into the Nansen Basin (~90 km), but maximum particle loads decreased to 2.6 ppm. Successive mixing[10,12] decreased BSBW signals, whereas particle discharge towards the seafloor reduced the particle load and its association with BSBW with increasing propagation distance. East of Vilkitzky Strait (Extended Data Fig. 5d,e), ~420 km downstream the first observation, maximum particle signals decreased to 1 ppm while the association with decreasing BSBW signatures reduced further. Ongoing degradation and remineralization, evident in the observations of increased zooplankton abundances (Extended Data Fig. 1f) and heterotrophic indicator species and ammonium oxidizing *Nitrococcacceae* in genomic sequences of particle-associated microbes within BSBW (Supplementary Table 1) further reduced the POC load and caused discharge of dissolved carbon and nutrients into surrounding waters. Finally, north of the central Laptev Sea (Extended Data Fig. 5f,g), distinct BSBW signals were absent, and maximum particle loads of 0.4 ppm were almost exclusively located below the 27.97 kg m^{-3} isopycnal at ~1,500 m. BSBW-driven particle injection thus represents a pathway for organic matter from the shelf over ~1,000 km into the Eurasian Basin (Fig. 3) and provides a food source for the deep sea community, which previously could not be explained by vertical export of local sources alone[9].

Quantifying BSBW-driven deep carbon injection

To estimate the spatial POC distribution, we scaled up our high-resolution sensor data with discrete size-fractionated POC measurements (Extended Data Fig. 6 and Extended Data Table 2). These calculations revealed maximum POC concentrations of 26.5 mg C m^{-3} in the plume north of Severnaya Zemlya (Extended Data Fig. 7), with a contribution of ~2/3 by the particle size fraction <0.1 mm (on average 12.4 mg C m^{-3} and 7.0 mg C m^{-3} for <0.1 mm and >0.1 mm, respectively). We further calculated the along-slope lateral POC flux based on the BSBW current velocity of 0.063 m s^{-1} on the day of sampling

as measured by Acoustic Doppler Current Profiler and Rotor Current Meter within this transect (Methods). Calculations yielded average total lateral carbon fluxes of 84.3–117.6 g C m^{-2} d^{-1} within BSBW (<0.1 mm: 56.7–72.7 g C m^{-2} d^{-1}, >0.1 mm: 27.6–45.1 g C m^{-2} d^{-1}), while integration over the vertical BSBW area of 19.5 km^2 resulted in a total lateral transport of 2.06 kt C d^{-1}. Including particles >0.1 mm, which were observed to slowly sink out of the BSBW, increased the lateral flux to 2.33 kt C d^{-1}. This value is equivalent to 8.55 kt CO$_2$, which equals the daily emission of 2–3 average-sized coal-fired power plants e.g. as reported for China (3.6 kt CO$_2$ d^{-1} (ref.[33])).

Temporal trends and implications for polar carbon budgets

Seasonal and inter-annual changes in carbon fixation[34,35] and BSBW production[10,13,36] could cause fluctuations of the injected POC into the deep sea. To resolve those trends, we applied the biogeochemical Regulated Ecosystem Model (REcoM2[37]) coupled to FESOM. The model was evaluated by comparing the spatial POC distribution from the field with the respective values from the model, showing that it successfully reproduced the process of dense water formation and subduction, driving particle injection and transport towards north of Severnaya Zemlya (Extended Data Fig. 8e,g). However, the location of the modelled POC plume was ~200 m shallower, and concentrations were generally approximately ten times lower (~2.5 mg C m^{-3}) than the field observations. This discrepancy could be explained by the temperature bias in the underlying FESOM model, causing a reduced density and export depth of the produced bottom water but also a reduced injection flux. Additionally, REcoM2 does not include resuspension processes, which probably play an important role for carbon transport on the shelf and might lead to an underestimation of the transported POC load. These results indicate that the process of dense water-driven particle injection could qualitatively be well reproduced by REcoM2, making it a suitable tool to resolve temporal trends of carbon outflow.

Model results revealed that pulses of carbon-rich dense water leave the shelf during and following the productive season in the second half of every year (Fig. 4).
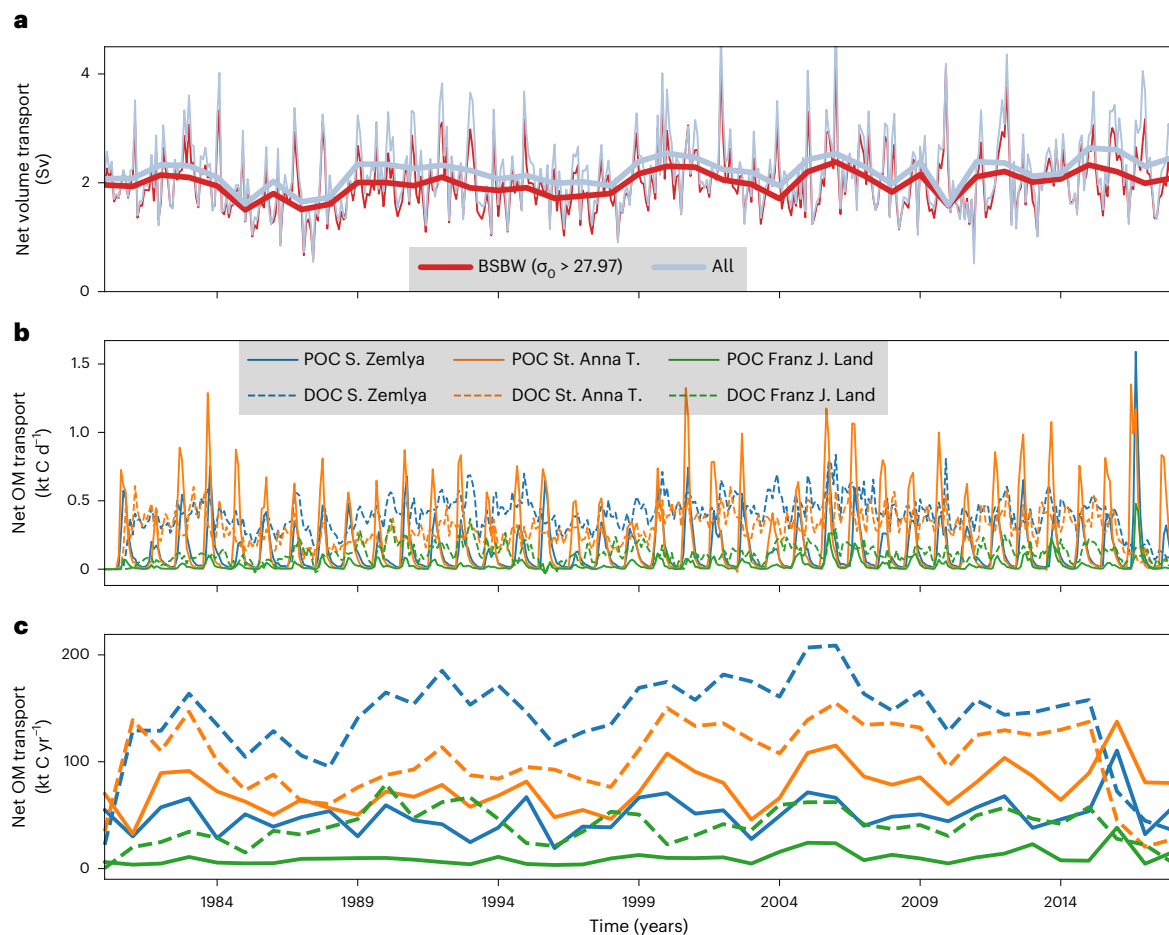
Fig. 4 | Time series of cross-sectional transport of water masses and organic carbon from the FESOM–REcoM2 model run. a, Total (grey) and BSBW (potential density anomaly [σ0] >27.97; red) transport through St. Anna Trough. **b,c**, Daily (**b**) and total annual (**c**) transport of dissolved (dashed lines) and particulate (solid lines) organic matter (OM) within BSBW through sections north of Franz Josef Land (green; Franz J. Land), St. Anna Trough (orange; St. Anna T.) and north of Severnaya Zemlya (blue; S. Zemlya).

Compared with the field-based POC flux north of Severnaya Zemlya (2.33 kt d^{-1}), the respective modelled flux for August 2018 was approximately ten times lower (~0.2 kt C d^{-1}, factor 11.68) but only approximately five times lower when using September outputs (0.52 kt C d^{-1}, factor 4.46). The limited temporal coverage of our field data did not allow an evaluation of seasonal outflow patterns, and in turn, a possible mismatch of POC transport peaks cannot be excluded. Moreover, in periods between POC outflow peaks, modelled fluxes almost reached undetectable levels, but resuspension of deposited material not represented in the model may cause limited fluxes to occur in between bloom phases in reality. Annual flux estimates including seasonal fluctuations were calculated by correcting modelled annual fluxes with daily flux discrepancy factors between model and field estimations. North of Severnaya Zemlya, this estimation revealed 0.26–0.67 Mt C yr^{-1}, while in total up to ~1 Mt C yr^{-1} might get transported out of St. Anna Trough (0.35–0.94 Mt C yr^{-1}). This value would increase the total POC sequestration of the Barents Sea by ~1/3, considering a previously assumed burial of 2.8 Mt C yr^{-1} in shelf sediments only[35]. Moreover, it is equivalent to 3.6 Mt CO$_2$ yr^{-1} or ~3% of the total Barents Sea CO$_2$ uptake[14,38], which would retain the CO$_2$ emission of a low-emitting country, such as Iceland (3.7 Mt CO$_2$ yr^{-1}) (ref. [39]) from the atmosphere on millennial time scales[40] due to the slow circulation of Arctic deep waters. In addition, elevated fluxes of dissolved organic carbon (DOC), which were not quantified in the field, also could be observed in the REcoM2 results (Fig. 4b), where annual total DOC fluxes

fluctuated between 50% and 200% of the annual POC fluxes (Fig. 4c), promoting the role as a carbon sink.

Our FESOM model results revealed a relatively stable annual dense water outflow volume of ~2 Sv out of St. Anna Trough between 1980 and 2018 (Fig. 4a). At the same time and location, REcoM2 results showed the POC outflow to be slightly increasing (~0.05 Mt C yr^{-1} to ~0.07 Mt C yr^{-1}). This development could be explained by a higher biological production due to increased light and nutrient availability as a result of less sea ice cover and stratification that already more than doubled between 1989 and 2017 as reported based on satellite data[41]. With ongoing reduction of sea ice cover, however, dense water formation on the shelf also might decrease in the future[36], which would reduce the amount and the injection depth of carbon drastically and, in turn, also the retention time. Although we could not report this scenario in our model, negative feedback effects, and hence an amplification of global warming, cannot be excluded because underlying field measurements are scarce in this region.

We could show that the co-location of dense water formation and transport with elevated biological production in the Barents Sea impacts the carbon budget of the Arctic Ocean by retaining substantial amounts of carbon in the deep Nansen Basin while providing a food source for deep sea organisms. The Barents Sea, however, is not the only shelf region with such co-location. For example, the Sea of Okhotsk, the Bering Sea or around northern Greenland[19,42] and, in particular, the Antarctic Ross[43] and Weddell seas[44–46] are characterized by dense

water formation and primary production, and it is therefore probable that high carbon injection rates also occur there as well. Moreover, high-density bottom waters produced around Antarctica[47] can lead to even deeper injection with longer retention times than reported here for the Arctic Ocean.

Polar regions are currently changing dramatically, and feedback effects of global warming might lead to even higher global mean temperatures in the future[48]. The scarcity of measurements in dense water outflow regions leads to uncertainties about injection systems within polar regions. A future reduction of dense water formation and hence a reduced transport of carbon from the atmosphere could result in a cumulative effect and a so far unconstrained amplification of global warming, which urgently calls for detailed studies of such systems.

Online content

Any methods, additional references, Nature Portfolio reporting summaries, source data, extended data, supplementary information, acknowledgements, peer review information; details of author contributions and competing interests; and statements of data and code availability are available at https://doi.org/10.1038/s41561-022-01069-z.

References

1. Hoegh-Guldberg, O. et al. Chapter 3: Impacts of 1.5ºC Global Warming on Natural and Human Systems. In *Special Report on Global Warming of 1.5 °C* (eds. Masson-Delmotte, V. et al.) https://doi.org/10.1017/9781009157940.005 (Camebridge Univ. Press 2022).
2. Bindoff, N. L. et al. Chapter 5: Changing Ocean, Marine Ecosystems, and Dependent Communities. In *IPCC Special Report on the Ocean and Cryosphere in a Changing Climate* (eds. Pörtner, H.-O. et al.) https://doi.org/10.1017/9781009157964.007 (Cambridge Univ. Press, 2019).
3. Watson, A. J. et al. Revised estimates of ocean-atmosphere CO_2 flux are consistent with ocean carbon inventory. *Nat. Commun.* **11**, 4422 (2020).
4. Ducklow, H. W. & Buesseler, K. O. Upper ocean carbon export and the biological pump. *Oceanography.* https://doi.org/10.5670/oceanog.2001.06 (2001).
5. Martin, J. H., Knauer, G. A., Karl, D. M. & Broenkow, W. W. VERTEX: carbon cycling in the northeast Pacific. *Deep-Sea Res.* **34**, 267–285 (1987).
6. Mathis, J. T., Pickart, R. S., Hansell, D. A., Kadko, D. & Bates, N. R. Eddy transport of organic carbon and nutrients from the Chukchi Shelf: impact on the upper halocline of the western Arctic Ocean. *J. Geophys. Res.* https://doi.org/10.1029/2006JC003899 (2007).
7. Lepore, K., Moran, S. B. & Smith, J. N. ^{210}Pb as a tracer of shelf–basin transport and sediment focusing in the Chukchi Sea. *Deep Sea Res. Part II* **56**, 1305–1315 (2009).
8. Forest, A. et al. Particulate organic carbon fluxes on the slope of the Mackenzie Shelf (Beaufort Sea): physical and biological forcing of shelf-basin exchanges. *J. Mar. Syst.* **68**, 39–54 (2007).
9. Wiedmann, I. et al. What feeds the benthos in the Arctic basins? Assembling a carbon budget for the deep Arctic ocean. *Front. Mar. Sci.* https://doi.org/10.3389/fmars.2020.00224 (2020).
10. Rudels, B. et al. Evolution of the Arctic Ocean boundary current north of the Siberian shelves. *J. Mar. Syst.* **25**, 77–99 (2000).
11. Dmitrenko, I. A. et al. Atlantic water flow into the Arctic Ocean through the St. Anna Trough in the northern Kara Sea. *J. Geophys. Res. Oceans* **120**, 5158–5178 (2015).
12. Rudels, B. et al. Circulation and transformation of Atlantic water in the Eurasian Basin and the contribution of the Fram Strait inflow branch to the Arctic Ocean heat budget. *Prog. Oceanogr.* **132**, 128–152 (2015).
13. Ivanov, V. V. & Shapiro, G. I. Formation of a dense water cascade in the marginal ice zone in the Barents Sea. *Deep Sea Res. Part I* **52**, 1699–1717 (2005).
14. Yasunaka, S. et al. Arctic Ocean CO_2 uptake: an improved multiyear estimate of the air–sea CO_2 flux incorporating chlorophyll a concentrations. *Biogeosciences* **15**, 1643–1661 (2018).
15. Arrigo, K. R. & van Dijken, G. L. Continued increases in Arctic Ocean primary production. *Prog. Oceanogr.* **136**, 60–70 (2015).
16. Slagstad, D., Wassmann, P. F. J. & Ellingsen, I. Physical constrains and productivity in the future Arctic Ocean. *Front. Mar. Sci.* **2**, 311 (2015).
17. Picheral, M. et al. The Underwater Vision Profiler 5. An advanced instrument for high spatial resolution studies of particle size spectra and zooplankton. *Limnol. Oceanogr. Methods* **8**, 462–473 (2010).
18. Wang, Q. et al. The Finite Element Sea Ice-Ocean Model (FESOM) v.1.4: formulation of an ocean general circulation model. *Geosci. Model Dev.* **7**, 663–693 (2014).
19. Tremblay, J.-E. & Smith, W. O. in *Elsevier Oceanography Series: Polynyas: Windows to the World* (eds Smith, W. O. & Barber, D. G.) Ch. 8 (Elsevier, 2007).
20. Makarevich, P. R. The primary production of the Barents Sea. *Vestnik of MGTU* https://doi.org/10.21443/1560-9278 (2012).
21. Reigstad, M., Carroll, J., Slagstad, D., Ellingsen, I. & Wassmann, P. Intra-regional comparison of productivity, carbon flux and ecosystem composition within the northern Barents Sea. *Prog. Oceanogr.* **90**, 33–46 (2011).
22. Wassmann, P., Slagstad, D., Riser, C. W. & Reigstad, M. Modelling the ecosystem dynamics of the Barents Sea including the marginal ice zone. *J. Mar. Syst.* **59**, 1–24 (2006).
23. Degen, R. et al. Patterns and drivers of megabenthic secondary production on the Barents Sea shelf. *Mar. Ecol. Prog. Ser.* **546**, 1–16 (2016).
24. Reigstad, M., Wexels Riser, C., Wassmann, P. & Ratkova, T. Vertical export of particulate organic carbon: attenuation, composition and loss rates in the northern Barents Sea. *Deep Sea Res. Part II* **55**, 2308–2319 (2008).
25. Shevchenko, V. P., Ivanov, G. & Zernova, V. V. Chapter *Vertical particle fluxes in the St. Anna Trough and in the eastern Barents Sea in August-September 1994* in *Modern and Late Quaternary Depositional Environment of the St. Anna Trough Area, Northern* Kara Sea(eds Stein, R. et al.) (Reports on Polar Research, 1999) 46-54.
26. Furevik, T. & Foldvik, A. Stability at M_2 critical latitude in the Barents Sea. *J. Geophys. Res.* **101**, 8823–8837 (1996).
27. Marin, B. & Melkonian, M. Molecular phylogeny and classification of the Mamiellophyceae class. nov. (Chlorophyta) based on sequence comparisons of the nuclear- and plastid-encoded rRNA operons. *Protist* **161**, 304–336 (2010).
28. Trudnowska, E. et al. Marine snow morphology illuminates the evolution of phytoplankton blooms and determines their subsequent vertical export. *Nat. Commun.* **12**, 2816 (2021).
29. Martiny, A. C. et al. Strong latitudinal patterns in the elemental ratios of marine plankton and organic matter. *Nat. Geosci.* **6**, 279–283 (2013).
30. Martiny, A. C., Vrugt, J. A., Primeau, F. W. & Lomas, M. W. Regional variation in the particulate organic carbon to nitrogen ratio in the surface ocean. *Glob. Biogeochem. Cycles* **27**, 723–731 (2013).
31. Crawford, D. W. et al. Low particulate carbon to nitrogen ratios in marine surface waters of the Arctic. *Glob. Biogeochem. Cycles* **29**, 2021–2033 (2015).
32. Passow, U. Transparent exopolymer particles (TEP) in aquatic environments. *Prog. Oceanogr.* **55**, 287–333 (2002).
33. Wu, N. et al. Daily emission patterns of coal-fired power plants in China based on multisource data fusion. *ACS Environ. Au* **2**, 363–372 (2022).
34. Sakshaug, E. Biomass and productivity distributions and their variability in the Barents Sea. *ICES J. Mar. Sci.* **54**, 341–350 (1997).

35. Pathirana, I., Knies, J., Felix, M. & Mann, U. Towards an improved organic carbon budget for the western Barents Sea shelf. *Clim. Past* **10**, 569–587 (2014).

36. Oziel, L., Sirven, J. & Gascard, J.-C. The Barents Sea frontal zones and water masses variability (1980–2011). *Ocean Sci.* **12**, 169–184 (2016).

37. Schourup-Kristensen, V., Sidorenko, D., Wolf-Gladrow, D. A. & Völker, C. A skill assessment of the biogeochemical model REcoM2 coupled to the finite element sea-ice ocean model (FESOM 1.3). *Geosci. Model Dev.* https://doi.org/10.5194/gmdd-7-4153-2014 (2014).

38. Manizza, M., Menemenlis, D., Zhang, H. & Miller, C. E. Modeling the recent changes in the Arctic Ocean CO_2 sink (2006–2013). *Glob. Biogeochem. Cycles* **33**, 420–438 (2019).

39. Friedlingstein, P. et al. Global carbon budget 2020. *Earth Syst. Sci. Data* **12**, 3269–3340 (2020).

40. Armstrong, C. W. et al. Valuing blue carbon changes in the Arctic Ocean. *Front. Mar. Sci.* https://doi.org/10.3389/fmars.2019.00331 (2019).

41. Dalpadado, P. et al. Climate effects on temporal and spatial dynamics of phytoplankton and zooplankton in the Barents Sea. *Prog. Oceanogr.* **185**, 102320 (2020).

42. Ohshima, K. I., Nihashi, S. & Iwamoto, K. Global view of sea-ice production in polynyas and its linkage to dense/bottom water formation. *Geosci. Lett.* https://doi.org/10.1186/s40562-016-0045-4 (2016).

43. Arrigo, K. R., van Dijken, G. & Long, M. Coastal Southern Ocean: a strong anthropogenic CO_2 sink. *Geophys. Res. Lett.* https://doi.org/10.1029/2008GL035624 (2008).

44. Huhn, O. et al. Evidence of deep- and bottom-water formation in the western Weddell Sea. *Deep Sea Res. Part II* **55**, 1098–1116 (2008).

45. von Bröckel, K. Primary production data from the south-eastern Weddell Sea. *Polar Biol.* **4**, 75–80 (1985).

46. Gleitz, M., Bathmann, U. & Lochte, K. Build-up and decline of summer phytoplankton biomass in the eastern Weddell Sea, Antarctica. *Polar Biol.* https://doi.org/10.1007/BF00240262 (1994).

47. Orsi, A. H., Johnson, G. C. & Bullister, J. L. Circulation, mixing, and production of Antarctic Bottom Water. *Prog. Oceanogr.* **43**, 55–109 (1999).

48. Natali, S. M. et al. Permafrost carbon feedbacks threaten global climate goals. *Proc. Natl Acad. Sci. USA* https://doi.org/10.1073/pnas.2100163118 (2021).

Methods

Cruise description and sensor set-up

Data and samples were collected during the research campaign ARCTIC2018 in the Nansen Basin and Laptev Sea onboard RV Akademik Tryoshnikov from 18 August to 29 September 2018. Conductivity, temperature and depth profiles (CTD; SBE 9plus, Sea-Bird Electronics) including fluorometer (ECO Fl, Wetlabs) and turbidity data (ECO BB, Wetlabs) were acquired at each station[49,50]. An Underwater Vision Profiler (UVP 5hd; Hydroptic) was mounted on the CTD frame and acquired particle data and images with a maximum frequency of 20 Hz during descent.

Size-fractionated particulate organic carbon and nitrogen sampling and measurements

Size-fractionated POC and particulate organic nitrogen (PON) sampling was accomplished by filtering up to 60 l of sample water directly from the Niskin bottles through 0.1 mm nylon mesh filters (Millipore). Subsequently, material >0.1 mm on the mesh filters was rinsed off using sterile filtered seawater (0.2 μm) and filtered onto 0.8 μm GFF filters (Whatman). 2 l of the corresponding filtrate from 0.1 mm nylon mesh filters was filtered onto 0.8 μm GFF filters (Whatman) to assess the size fraction <0.1 mm. To reduce fragmentation of fragile aggregates >0.1 mm into the filtrate and thus the particle pool <0.1 mm, water flow during mesh filtration was adjusted to minimum. Moreover, material was rinsed off from the mesh very thoroughly to avoid loss of material >0.1 mm. Samples were stored at −80 °C before removing carbonates by acidification and tin encapsulation. Measurements of C and N content of the processed samples were carried out using an element analyser (Euro EA 3000 Elemental Analyser, Eurovector).

Size-fractionated DNA sampling for amplicon 16S and 18S rRNA gene polymerase chain reaction and sequencing

Size-fractionated DNA sampling was accomplished analogously to POC and PON sampling. The particle size fraction >0.1 mm was sampled by filtering approximately 10 l of sample water slowly from the Niskin bottle onto 0.1 mm nylon mesh (Millipore) before resuspension with sterile filtered (0.2 μm) seawater and filtration onto 0.22 μm filters (Sterivex, Millipore) using a peristaltic pump (Masterflex, Cole-Parmer). The size fraction <0.1 mm was sampled by filtering 2 l of the filtrate directly onto 0.22 μm filters. Filters were kept at −80 °C until opening them in the lab followed by DNA extraction using the DNeasy PowerWater Kit (Qiagen) according to manufacturer's instructions. The number of the resulting extracts (n) for 16S and 18S sequencing was 24 for the particle size fraction <0.1 mm and 23 for the size fraction >0.1 mm, respectively. DNA extracts were stored at −20 °C before generation of prokaryotic and eukaryotic amplicon sequences targeting the 16S rRNA (27F–519R (ref. [51])) and 18S rRNA gene (TAReuk454FWD1–TAReukREV3 (ref. [52])), respectively. Amplicon libraries were created following standard protocols of amplicon library preparation (16S Metagenomic Sequencing Library Preparation, Illumina, part number 15044223 Rev. B; Appendix B). Both 16S and 18S rRNA polymerase chain reaction libraries were sequenced using 250 base pairs paired-end sequencing with a MiSeq Sequencer (Illumina).

Analyses of amplicon sequence data and statistical analysis

Amplicon sequence variant (ASV) tables were constructed using the DADA2 pipeline v. 1.15.1 (ref. [53]) with standard parameters and additional primer trimming using Cutadapt v. 1.18 (ref. [54]). Sequencing statistics for remaining sequences after each filtering step are reported in Supplementary Tables 2 and 3. Sequences were taxonomically assigned outside DADA2 using the SilvaNGS v. 1.4 (ref. [55]) pipeline for 16S rRNA gene data with the similarity threshold set to 1. Reads were aligned using SINA v. 1.2.10 (ref. [56]) and classified using BLASTn v. 2.2.30 (ref. [57]) with the Silva database v. 132 as a reference database. 18S rRNA gene amplicons were assigned using the 'feature-classifier' v. 2019.7.0 (from package 'q2-feature-classifier' v. 2019.7.0) in QIIME 2 (ref. [58]) and the pr2 database v. 4.12 (ref. [59]) as a reference database.

The ASV tables were Hellinger transformed to stabilize the variance in the sequence count data for beta dispersion and PERMANOVA analyses using the decostand() function in zCompositions (rowsum cut-off = 3). Environmental metadata were z-scored (mean of data variable shifted to 0) for comparable metadata analysis.

To examine microbial community dissimilarity between groups ('outside plume', 'plume'), we performed a principal coordinate analysis (PCoA); we calculated beta dispersion of sites based on Bray–Curtis dissimilarity analysis of Hellinger-transformed ASV tables. PCoA eigenvalues were used to examine variation captured in PCoA axes. Differences of microbial communities between groups were tested with a permutational MANOVA (PERMANOVA[60]) on the Hellinger-transformed ASV tables using the adonis2() function in vegan (v. 2.5.6).

UVP particle and image data processing

Pre-processing of particle and image data from the UVP was accomplished using the software Zooprocess[61]. Calculation of particle volume per sample volume and data binning into 5 m depth bins and standardized, evenly spaced size classes between 0.102 mm and 2.05 mm ESD (further 0.1 mm and 2 mm) on a natural logarithmic scale was carried out using standard procedures[62]. Classification and validation of acquired images (>0.8 mm) was accomplished using the web-based application Ecotaxa[63]. Images were individually classified with the assistance of machine learning classifiers into respective groups of living zooplankton and non-living marine snow. Marine snow was further classified into distinct groups using k-means clustering of principal component analysis (PCA) coordinates of morphological features of the detritus images as described elsewhere[28].

Maps were created using Ocean Data View[64] and the International Bathymetric Chart of the Arctic Ocean (IBCAO 3 (ref. [65])). The 3D overview of the particle volume distribution in the Nansen and Amundsen basins shown in Fig. 3 was created in PyGMT v. 0.6.1 (refs. [66,67]) using the SRTM15+ v. 2.4 grid[68] and surface gridding[69].

Estimating POC concentration using turbidity, fluorescence and optical particle data

To visualize high-resolution POC concentrations and to calculate total POC flux throughout the bottom water plume, we scaled up size-fractionated POC measurements using CTD-based fluorescence and turbidity data and optical particle concentration and size distribution data from the UVP. Regressions were carried out using the statsmodels (v. 0.12.2) Python module[70].

High-resolution POC concentrations within the UVP size fraction >0.1 mm ESD were estimated using the pattern of the particle size distribution, total particle volume and POC concentration of the sampled fraction >0.1 mm ($n = 92$). Only particle volumes of size classes up to 2 mm ESD were included in the estimation to eliminate rare but massive outliers, for example, due to large zooplankton. The pattern of the particle size distribution was described by the two coefficients a and b of the power law function ($f_{(x)} = ax^b$) fitted over the relative cumulative particle size class distribution (cumulative volume: total volume; Vol_{cum}:Vol_{tot}) using ordinary least squares (OLS) regression (Extended Data Fig. 6a,b). To optimize regression and to enable zero-based power law fitting, centres of the respective ESD size bins (in μm) were used and transformed before regression (subtracted by the smallest size bin centre value of 115 μm; ESD_t) to eliminate the offset below the UVP detection limit. Measured POC concentrations >0.1 mm ESD where then correlated to the total particle volume 0.1–2 mm ESD and the calculated coefficients a and b (Extended Data Fig. 6c). The regression was achieved using a generalized linear model based on the gamma distribution model family, logarithmic link function and iteratively reweighted least squares (Extended Data Table 2). Resulting intercept and coefficients were then used to estimate POC concentrations

>0.1 mm for each UVP depth bin, following OLS regression of the respective zero-transformed cumulated volumetric particle size distribution as described above.

High-resolution POC estimation of the fraction below the UVP size threshold of 0.1 mm was achieved by correlating the POC concentrations of the sampled fraction <0.1 mm ESD (n = 92) with CTD-based turbidity and chlorophyll a fluorescence sensor data of the respective sampling location and depth (Extended Data Fig. 6d). Therefore, a robust linear regression model based on iteratively reweighted least squares including Andrew's Wave M-estimator as weight function was used (Extended Data Table 2). The resulting intercept and coefficients of this regression were then used to estimate POC concentrations <0.1 mm ESD for each CTD data point.

Fitting of the resulting estimates of the POC load <0.1 mm and >0.1 mm ESD are presented as the difference between the measured and estimated POC concentration for the respective sampling location and depth (Extended Data Fig. 6e). Almost all larger outliers were located in the euphotic zone, pointing towards non-matching locations of sampling and data acquisition due to the patchiness of the POC distribution in this zone. Nevertheless, about 80% of the estimates showed a difference below 10 mg m^{-3}, representing a relatively robust regression considering the different nature of the approaches, the fact that data acquisition of CTD and UVP occurred during descent and POC sampling during ascent with wind drift in between and that no organisms were picked out of the samples.

Definition of BSBW, current velocities and data processing

BSBW was defined based on the transformation characteristics of Atlantic waters of the West Spitsbergen current region. Being denser than waters in the intermediate density layer and less saline than dense Atlantic water from Fram Strait, transformed BSBW north of Severnaya Zemlya was characterized by absolute salinities <35.06 g kg^{-1} and potential density anomalies >27.97 kg m^{-3} after leaving the Barents Sea shelf through St. Anna Trough. Units used for definition were based on the Thermodynamic Equations Of Seawater–2010[71] and calculated using, for example, the Python package gsw (v. 3.4.0).

The average ocean current velocity of the area covered by BSBW across the westernmost transect was estimated from Acoustic Doppler Current Profilers (ADCPs, Teledyne RDI) and rotor current meters (RCM) deployed in a high-resolution mooring array. The array consisted of seven moorings (AK1 to AK7) arranged perpendicular to the continental slope in water depths between 300 m (AK1) and 3,015 m (AK7) from August 2015 to September 2018 (E.R.-C. et al., manuscript in peer review). The sampling frequency for ADCPs and RCMs was 90 minutes and 120 minutes, respectively. The effects of the tide and inertial periods were removed with a six-day running average window, and temporal resolution was reduced to one day. Only velocity measurements located within the BSBW region were used (AK2 to AK5). RCM current records at AK4 and AK5 stopped on 31 January 2016 and 11 May 2017, respectively. These gaps in the time series were recovered by scaling velocities from the ADCPs. Before the current records stopped, correlation between time series from both instruments for the zonal and meridional components were 0.85–0.71 and 0.56–0.47 for AK4 and AK5, respectively. Currents from 20 August 2018 were aligned in the along-slope direction and used to represent the time period when the hydrographic transect was occupied. The velocity records in the area where BSBW occurred were horizontally interpolated and averaged. More detailed descriptions of deployment, water mass definition, calculation procedures and the resulting dataset will be published separately (E.R.-C. et al., manuscript in peer review).

Estimating BSBW-driven lateral POC flux in the westernmost transect closest to the St. Anna Trough outflow

BSBW-driven lateral POC flux was estimated for the westernmost transect closest to St. Anna Trough based on POC load estimations described above starting with the station-wise integration of POC contents within BSBW per m^2 water column. For each station of this transect, POC contents per m^2 BSBW per station were then multiplied by half of the distance to the nearest stations north- and southwards, respectively. No extrapolation towards the south of the southernmost and towards north of the northernmost station was calculated to perform a conservative flux estimation. The resulting POC content in the whole vertical area of BSBW was then multiplied by the BSBW current velocity (0.063 m s^{-1}) within the same transect and from the day of sampling (above). Finally, calculation of different time intervals (day, year) and average lateral flux per m^2 followed.

On the basis of the assumption that a fraction of POC > 0.1 mm ESD was transported into the area by BSBW but was dislocated due to gravitational settling (Fig. 1, Extended Data Fig. 1 and Extended Data Fig. 7), one can conclude that this material was also transported with the BSBW current velocity of 0.063 m s^{-1}. To obtain estimates of the potential additional fluxes by this material, we calculated the possible additional POC load as follows: maximum depth with increased POC concentration >0.1 mm below BSBW was calculated by identifying the depth for each station where ambient concentrations below BSBW were reached. Ambient concentrations were defined for each station as the average POC load >0.1 mm within 100 m above the BSBW subtracted by its standard deviation. Ambient concentrations were reached right below BSBW in all stations except for one station located at 82.11° N and 94.84° E. For this profile, POC concentrations >0.1 mm ESD were integrated over the layer below the depth of the last BSBW signal and the identified maximum depth. This POC load per m^2 water column was then multiplied by half the distances to the next two stations north- and southwards as described above and multiplied by the BSBW current velocity of 0.063 m s^{-1}.

FESOM modelling of current speeds and particle backtracking

To better understand the velocity structure in the northern Barents Sea, we used the velocity field from the Finite-Element Sea ice-Ocean Model v. 1.4 (FESOM 1.4 (ref. [18])). FESOM 1.4 is based on triangular unstructured meshes for both the ocean and sea ice components. The global model grid has 4.5 km resolution in the Arctic Ocean and 24 km in the North Atlantic. The model configuration used here was forced with atmospheric reanalysis data from JRA55-do v. 1.3 (ref. [72]) and reasonably represents the hydrography and velocity structure in the Arctic Ocean[73,74]. One should note that in the model, a known warm bias of around 1 °C relative to the Polar Science Center Hydrographic Climatology (PHC v. 3 (ref. [75])) was present in the Eurasian Basin of the Arctic Ocean (Fig. 4 in ref. [73]). Resulting water mass distribution, however, was similar to field observations, although the location of the dense water plume at the westernmost transect at ~90° E was slightly shallower (Fig. 1 and Extended Data Fig. 2). Following release depths for particle backtracking were adjusted accordingly to match the observed co-location of particle maxima with dense water.

A Lagrangian particle-tracking algorithm was used to determine the origin of representative particle classes observed at the continental shelf break. It has been successfully applied before to study the catchment area of sediment traps deployed in Fram Strait[76], the pathways of microplastic in the Arctic Ocean[77] and vertical microbial connectivity in Fram Strait[78]. Seventy particles were released at the respective depths of bottom water in the model within the westernmost transect of the plume observed in the field (95° E, 81.9° N–82.14° N), at 450 m, 500 m, 550 m, 600 m, 650 m, 700 m and 750 m depth (Extended Data Fig. 2c). Release was carried out every 14 days in 2018 and back tracked until they reached the ocean surface, resulting in 1,680 trajectories. A time step of 30 min was used for the trajectory calculations, yielding bi-hourly positions. The horizontal displacement of particles was computed with daily-averaged velocity fields from FESOM 1.4, and the vertical displacement was determined from constant sinking velocities measured for particle samples from Fram Strait[78]. The sinking velocity (v)

was computed with its empirical relationship to particle ESD described by the coefficients a and b of the power law function ($v = a(\text{ESD})^b$). We conducted backtracking model runs with sinking velocities representing non-ballasted ($a = 34.6$, $b = 1.39$), small (0.08 mm ESD) and large (0.5 mm ESD) particles ($v = 1.03$ m d^{-1} and 13.2 m d^{-1}, respectively) and small ballasted particles ($a = 94.58$, $b = 0.96$) with 0.08 mm ESD ($v = 8.58$ m d^{-1}). Selected numerical results are shown in Extended Data Table 1.

Evaluation of the injection process and seasonal and inter-annual trends using REcoM2

The Regulated Ecosystem Model (REcoM2) is a biogeochemical model describing the lower trophic levels of the marine Arctic ecosystem with one zooplankton class, the phytoplankton types diatoms and nanophytoplankton and one type of detritus[37]. It includes descriptions of the cycles of nitrogen, silicon and iron and the carbon cycle, whereas water mass and current properties are based on FESOM (above). The FESOM–REcoM2 set-up was run from 1980 to 2018. The first 25 years of the run have been validated by Schourup–Kristensen et al.[79], while the time-varying trends in Arctic nitrate supply are discussed in Oziel et al.[80].

Combining model and field data to estimate annual POC flux

To provide realistic annual POC flux estimations including seasonal outflow patterns, outputs from the REcoM2 model runs were corrected using flux calculations from the field (above). A correction factor for the model was created by dividing the monthly RECOM2 output of the average daily POC flux within BSBW of the westernmost field transect north of Severnaya Zemlya by the respective daily field data-based flux. Due to the fact that field data collection took place at the end of August (22 August) and that we could not exclude a temporal mismatch between peaks of field and model-based POC outflow from the shelf, we calculated this correction factor for August and September 2018, respectively. Annual REcoM2-based POC fluxes for the transects north of Severnaya Zemlya and St. Anna Trough were then multiplied by those two correction factors, resulting in a range of field data-corrected POC fluxes for those transects.

Data availability

CTD data are available on PANGEA[49] and the Arctic Data Center[50]. Detailed UVP image and particle data that support the findings are publicly available on EcoTaxa (https://ecotaxa.obs-vlfr.fr, project number 2463) and Ecopart (https://ecopart.obs-vlfr.fr; project number 239). Results of the PCA-based k-means clustering of detritus classes, depth-binned distributions of zooplankton and particle size classes and the measured POC/PON data and the resulting POC estimates are publicly available on the PANGAEA data repository (bundled in https://doi.org/10.1594/PANGAEA.947425, https://doi.org/10.1594/PANGAEA.947376 and https://doi.org/10.1594/PANGAEA.947381). Results of the 16S and 18S amplicon sequencing are deposited in the European Nucleotide Archive at EMBL-EBI under accession number PRJEB53455. Sequence data submission was done using the data brokerage service of the German Federation for Biological Data[81] in compliance with the Minimal Information about any (X) Sequence (MIxS) standard[82]. Results of the FESOM ocean current model and particle backtracking calculations are publicly available on Zenodo (https://doi.org/10.5281/zenodo.7085120). Curated REcoM2 model transect and time series data are publicly available on Zenodo (https://doi.org/10.5281/zenodo.7071160 and https://doi.org/10.5281/zenodo.7071083).

Code availability

Results were achieved using publicly available Python and R packages as mentioned in the Methods section. All scripts for POC estimations can be provided upon request.

References

49. Ivanov, V. Physical oceanography from CTD measurements during Akademik Tryoshnikov cruise AT2018 to the Arctic Ocean. *PANGAEA*. https://doi.org/10.1594/PANGAEA.905471 (2019).

50. Polyakov, I. & Rember, R. Conductivity, Temperature, Pressure (CTD) measurements from cast data taken in the Eurasian and Makarov basins, Arctic Ocean, 2018. Arctic Data Ceter https://doi.org/10.18739/A2X34MS0V (2019).

51. Parada, A. E., Needham, D. M. & Fuhrman, J. A. Every base matters: assessing small subunit rRNA primers for marine microbiomes with mock communities, time series and global field samples. *Environ. Microbiol.* **18**, 1403–1414 (2016).

52. Stoeck, T. et al. Multiple marker parallel tag environmental DNA sequencing reveals a highly complex eukaryotic community in marine anoxic water. *Mol. Ecol.* **19**, 21–31 (2010).

53. Callahan, B. J. et al. DADA2: high-resolution sample inference from Illumina amplicon data. *Nat. Methods* **13**, 581–583 (2016).

54. Martin, M. Cutadapt removes adapter sequences from high-throughput sequencing reads. *EMBnet J.* https://doi.org/10.14806/ej.17.1.200 (2011).

55. Quast, C. et al. The SILVA ribosomal RNA gene database project: improved data processing and web-based tools. *Nucleic Acids Res.* **41**, D590–D596 (2013).

56. Pruesse, E., Peplies, J. & Glöckner, F. O. SINA: accurate high-throughput multiple sequence alignment of ribosomal RNA genes. *Bioinformatics* **28**, 1823–1829 (2012).

57. Camacho, C. et al. BLAST+: architecture and applications. *BMC Bioinf.* **10**, 421 (2009).

58. Bokulich, N. A. et al. Optimizing taxonomic classification of marker-gene amplicon sequences with QIIME 2's q2-feature-classifier plugin. *Microbiome* **6**, 1–17 (2018).

59. Guillou, L. et al. The Protist Ribosomal Reference database (PR2): a catalog of unicellular eukaryote small sub-unit rRNA sequences with curated taxonomy. *Nucleic Acids Res.* **41**, D597–D604 (2013).

60. Anderson, M. J. A new method for non-parametric multivariate analysis of variance. *Austral Ecol.* **26**, 32–46 (2001).

61. Gorsky, G. et al. Digital zooplankton image analysis using the ZooScan integrated system. *J. Plankton Res.* **32**, 285–303 (2010).

62. Kiko, R. et al. A Global Marine Particle Size Distribution Dataset Obtained with the Underwater Vision Profiler 5. *Earth Syst. Data* **14**, 4315–4337 (2022).

63. Picheral, M., Colin, S. & Irisson, J.-O. EcoTaxa, a Tool for the Taxonomic Classification of Images. http://ecotaxa.obs-vlfr.fr (2017).

64. Schlitzer, R. Ocean Data View. https://odv.awi.de; https://doi.org/10013/epic.07f8e9e9-6111-47e9-a6dd-494af6f01c7b (2022).

65. Jakobsson, M. et al. The International Bathymetric Chart of the Arctic Ocean (IBCAO) version 3.0. *Geophys. Res. Lett.* https://doi.org/10.1029/2012GL052219 (2012).

66. Uieda, L. et al. PyGMT: a Python interface for the Generic Mapping Tools. *Zenodo* https://doi.org/10.5281/ZENODO.6426493 (2022).

67. Wessel, P. et al. The generic mapping tools version 6. *Geochem. Geophys. Geosyst.* **20**, 5556–5564 (2019).

68. Tozer, B. et al. Global bathymetry and topography at 15 Arc Sec: SRTM15+. *Earth Space Sci.* **6**, 1847–1864 (2019).

69. Smith, W. H. F. & Wessel, P. Gridding with continuous curvature splines in tension. *Geophysics* **55**, 293–305 (1990).

70. Seabold, S. & Perktold, J. Statsmodels: Econometric and statistical modeling with Python. In Proc. of the *9th Python in Science Conf.* (eds. van der Walt, S. & Millman, J.) https://doi.org/10.25080/Majora-92bf1922-012 (2010)

71. IOC, SCOR & IAPSO. *The International Thermodynamic Equation of Seawater–2010: Calculation and Use of Thermodynamic Properties* (UNESCO, 2010).

72. Tsujino, H. et al. JRA-55 based surface dataset for driving ocean–sea-ice models (JRA55-do). *Ocean Modell.* **130**, 79–139 (2018).

73. Wang, Q., Wekerle, C., Danilov, S., Wang, X. & Jung, T. A 4.5 km resolution Arctic Ocean simulation with the global multi-resolution model FESOM 1.4. *Geosci. Model Dev.* **11**, 1229–1255 (2018).

74. Wang, Q. et al. Intensification of the Atlantic water supply to the Arctic Ocean through Fram Strait induced by Arctic Sea ice decline. *Geophys. Res. Lett.* https://doi.org/10.1029/2019GL086682 (2020).

75. Steele, M., Morley, R. & Ermold, W. PHC: a global ocean hydrography with a high-quality Arctic Ocean. *J. Clim.* **14**, 2079–2087 (2001).

76. Wekerle, C. et al. Properties of sediment trap catchment areas in Fram Strait: results from lagrangian modeling and remote sensing. *Front. Mar. Sci.* https://doi.org/10.3389/fmars.2018.00407 (2018).

77. Tekman, M. B. et al. Tying up loose ends of microplastic pollution in the Arctic: distribution from the sea surface through the water column to deep-sea sediments at the HAUSGARTEN observatory. *Environ. Sci. Technol.* **54**, 4079–4090 (2020).

78. Fadeev, E. et al. Sea ice presence is linked to higher carbon export and vertical microbial connectivity in the Eurasian Arctic Ocean. *Commun. Biol.* **4**, 1255 (2021).

79. Schourup-Kristensen, V., Wekerle, C., Wolf-Gladrow, D. A. & Völker, C. Arctic Ocean biogeochemistry in the high resolution FESOM 1.4-REcoM2 model. *Prog. Oceanogr.* **168**, 65–81 (2018).

80. Oziel, L., Schourup-Kristensen, V., Wekerle, C. & Hauck, J. The pan-Arctic continental slope as an intensifying conveyer belt for nutrients in the central Arctic Ocean (1985–2015). *Glob. Biogeochem. Cycles* https://doi.org/10.1029/2021GB007268 (2022).

81. Diepenbroek, M. et al. Towards an integrated biodiversity and ecological research data management and archiving platform: the German federation for the curation of biological data (GFBio). In *Informatik 2014 - Big Data Komplexität meistern* (eds. Plödereder, E. et al.) GI-Edition: Lecture Notes in Informatics (LNI) – Proceedings 232: 1711-1724 (Köllen Verlag Bonn, 2014).

82. Yilmaz, P. et al. Minimum information about a marker gene sequence (MIMARKS) and minimum information about any (x) sequence (MIxS) specifications. *Nat. Biotechnol.* **29**, 415–420 (2011).

Author contributions

A.R. performed experimental design, field data and sample collection and preparation, UVP image validation and analyses and POC and PON measurements. N.L. participated in UVP image validation and data interpretation. E.T. performed PCA-based detritus classification. C.H. performed analyses of DNA amplicons and PCA-based community differences. E.R.-C., K.S. and M.J. ran, analysed and provided ADCP and RCM data. C.W. performed FESOM-based particle backtracking and current water mass transport calculations whereas L.O. and V.S.-K. performed biogeochemical REcoM2 model calculations. A.M.W., M.J., M.H.I. and V.V.P. coordinated this study and were involved in experimental design and data interpretation. A.R. prepared the manuscript with support and approval of all co-authors.

Competing interests

The authors declare no competing interests.

Additional information

Extended data is available for this paper at https://doi.org/10.1038/s41561-022-01069-z.

Supplementary information The online version contains supplementary material available at https://doi.org/10.1038/s41561-022-01069-z.
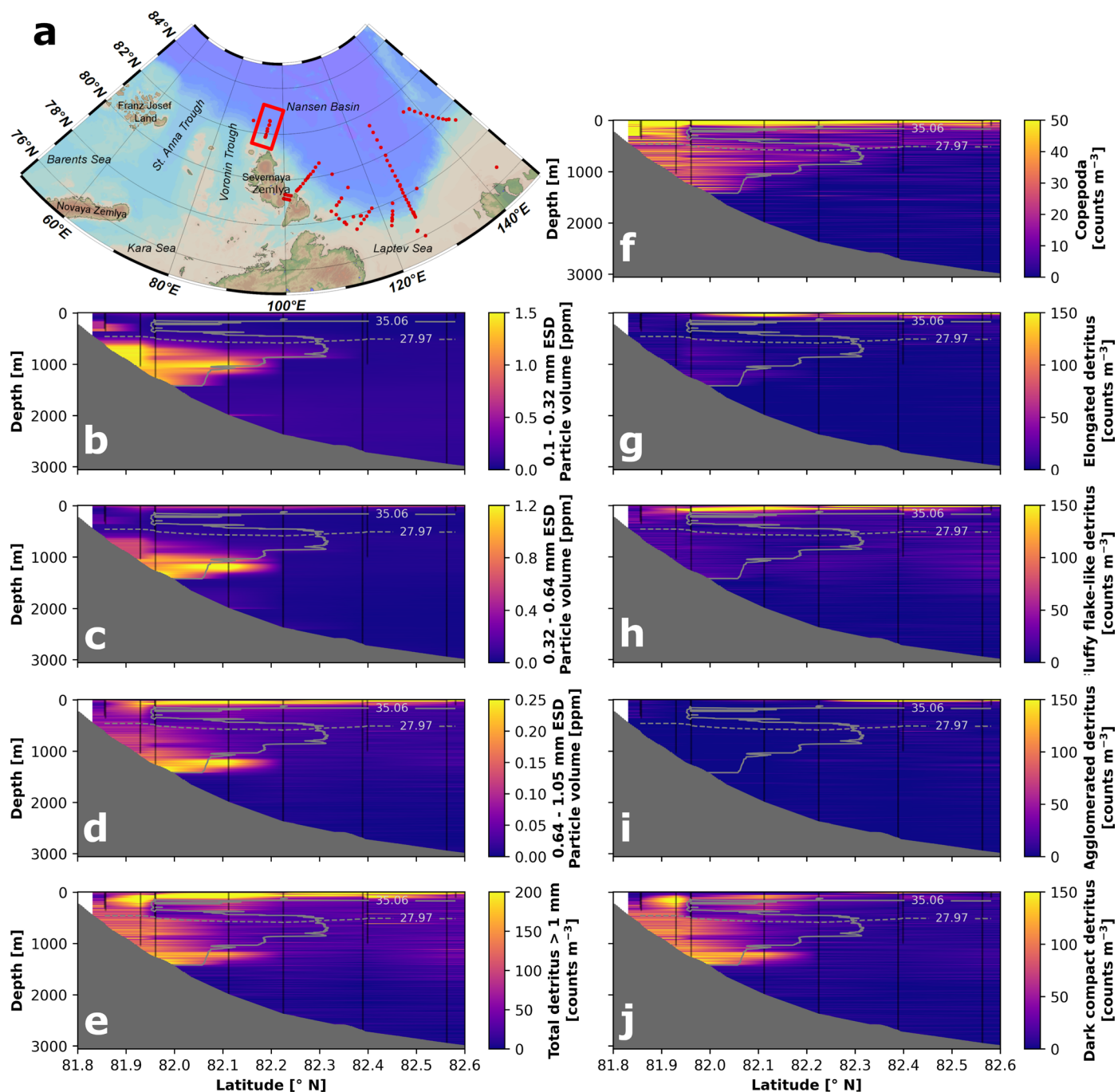
Correspondence and requests for materials should be addressed to Andreas Rogge.

Peer review information *Nature Geoscience* and the authors thank the anonymous reviewers for their contribution to the peer review of this work. Primary Handling editor: Rebecca Neely, in collaboration with the *Nature Geoscience* team.

**Reprints and permissions information** is available at www.nature.com/reprints.

Extended Data Fig. 1 | Detailed results of the UVP-based particle size distribution <0.8 mm and image analyses >0.8 mm. a, map of the research area including stations (red dots) and the shown transect (red rectangle) closest to the BSBW outflow region St. Anna Trough. **b**–**d**, spatial distribution of particle size classes <0.8 mm. **e**, **f**, distribution of imaged (>0.8 mm) (**e**) total detritus and (**f**) copepods. **g**–**f**, different imaged detritus classes >0.8 mm identified via PCA and *k*-means clustering. The areas above the solid (absolute salinity <35.06 g kg⁻¹) and below the dashed isolines (potential density anomaly >27.97 kg m⁻³) indicate BSBW. Please note the colour scale differences.
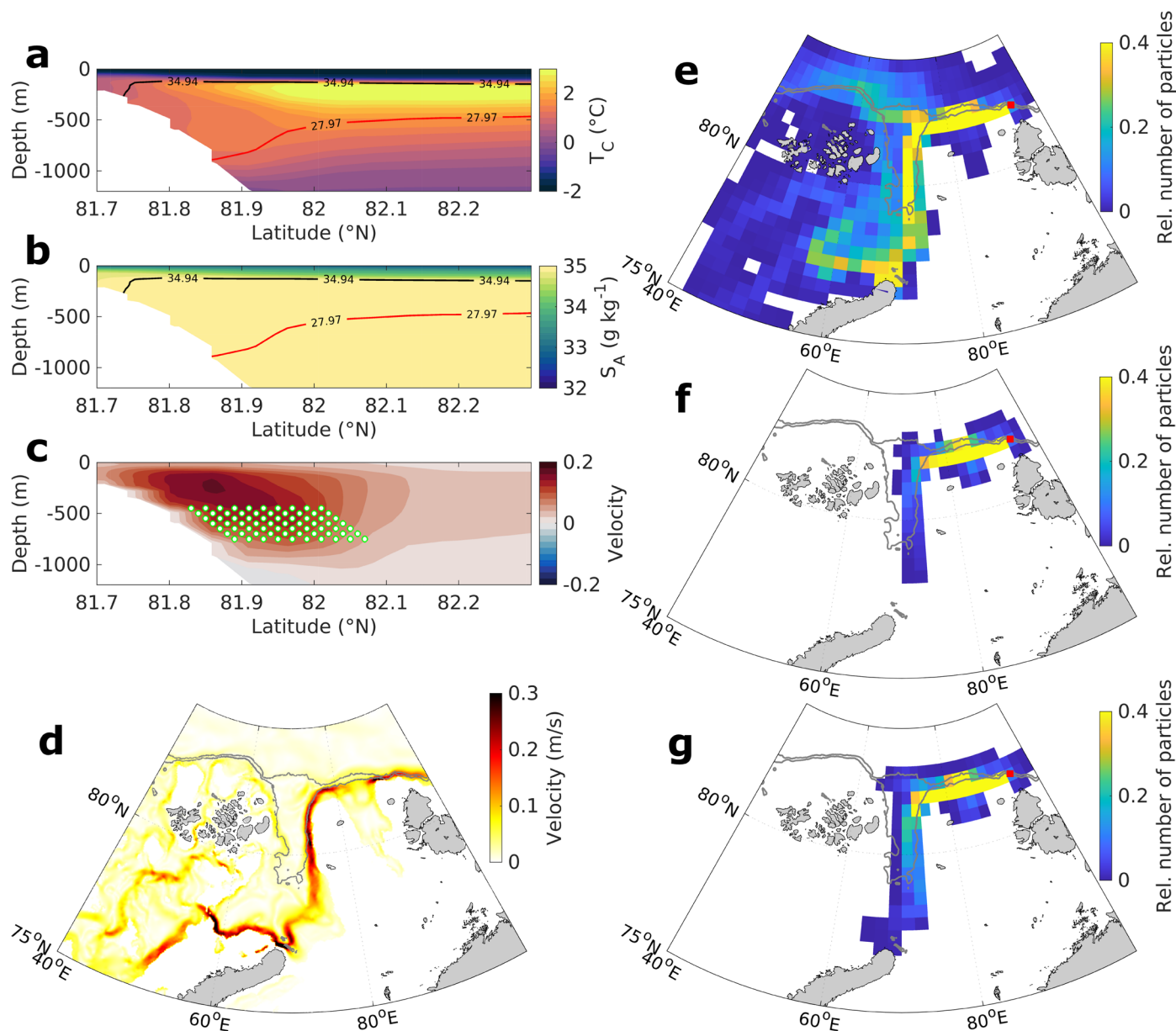
Extended Data Fig. 2 | Detailed results of ocean-sea ice modelling (FESOM)-based particle backtracking. a - c, annual mean water mass properties ([**a**] temperature and [**b**] practical salinity) and (**c**) zonal velocities from FESOM model run for the field transect North of Severnaya Zemlya. Green dots in **c** represent release locations for particle backtracking in dense BSBW. **d**, Mean ocean current velocity at 200 m depth simulated by FESOM and averaged over the years 1989–2018 visualizes the main outflow path of the Barents Sea branch of the Arctic Boundary Current from the Barents and Kara Sea shelf through St. Anna Trough. **e-g**, relative numbers of particles show the distribution of different representative particle classes released within the BSBW-plume of the field transect north of Severnaya Zemlya (red square) and back-tracked until reaching the surface. **e**, particles with 0.08 mm ESD and a sinking velocity of 1.03 m d^{-1} represent non-ballasted suspended particles <0.1 mm. **f**, particles with 0.5 mm ESD and a sinking velocity 13.2 m d^{-1} represent non-ballasted sinking particles >0.1 mm. **g**, particles with 0.08 mm ESD and a sinking velocity of 8.58 m d^{-1} represent ballasted particles <0.1 mm. Grey contour lines in **d-g** indicate the 500 m and 1,000 m isobaths, respectively.
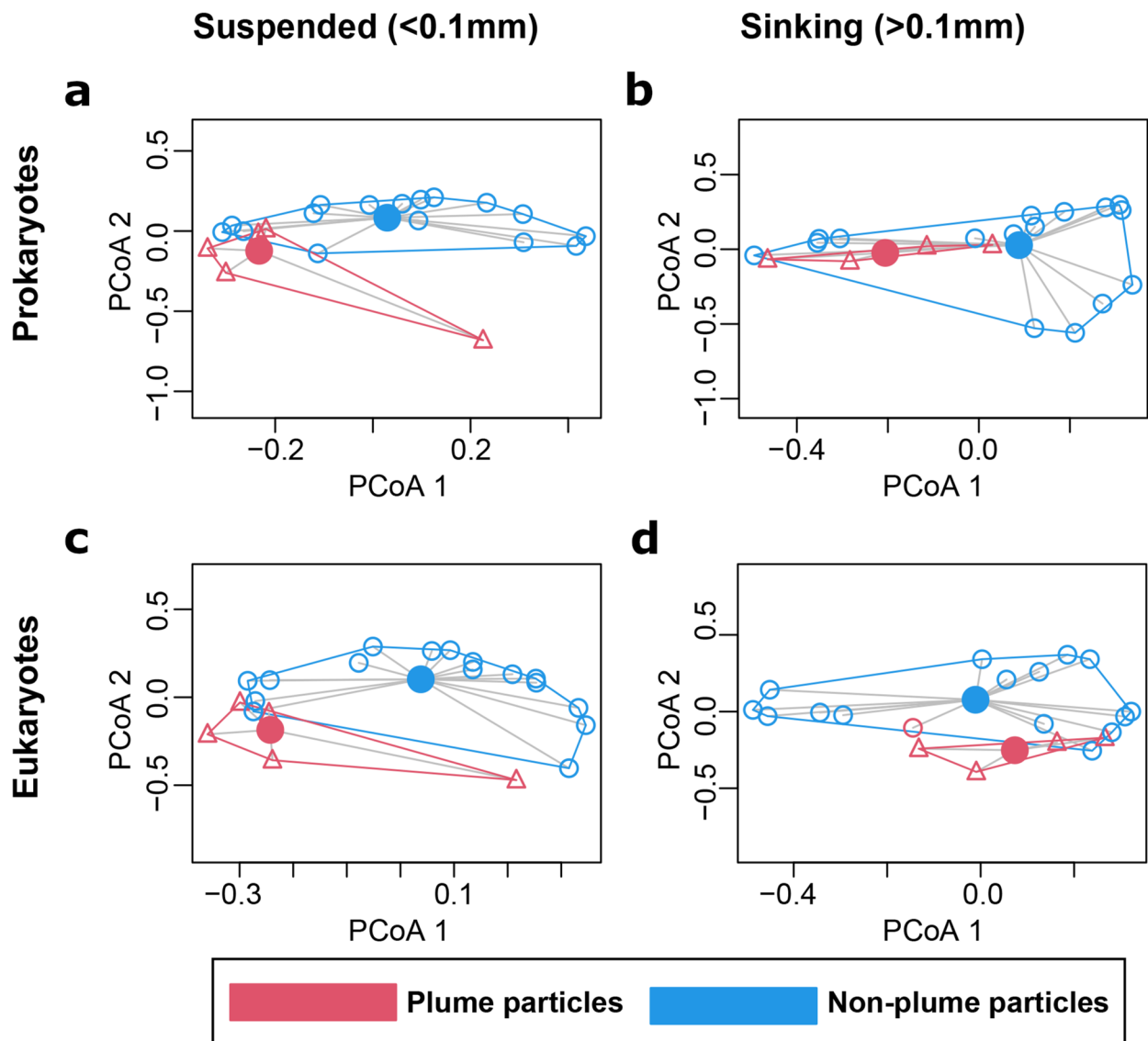
Extended Data Fig. 3 | Results of the principal coordinate analysis of the particle associated community composition between plume and non-plume (PERMANOVA, Hellinger transformed, 999 permutations). a, prokaryotic community differences (based on 16S rRNA genes) associated with particles <0.1 mm ESD. **b**, prokaryotic community differences (based on 16S rRNA genes) associated with particles >0.1 mm ESD. **c**, eukaryotic community differences (based on 18S rRNA genes) associated with particles <0.1 mm ESD. **d**, eukaryotic community differences (based on 18S rRNA genes) associated with particles >0.1 mm ESD. Weak relationships could be identified between plume and non-plume particle-associated microbes within sinking particles ($P = 0.019$, $R^2 = 0.102$ for prokaryotes, and $P = 0.032$, $R^2 = 0.082$ for eukaryotes), but correlations were stronger within suspended particles ($P = 0.007$, $R^2 = 0.123$ for prokaryotes, and $P = 0.002$, $R^2 = 0.117$ for eukaryotes).
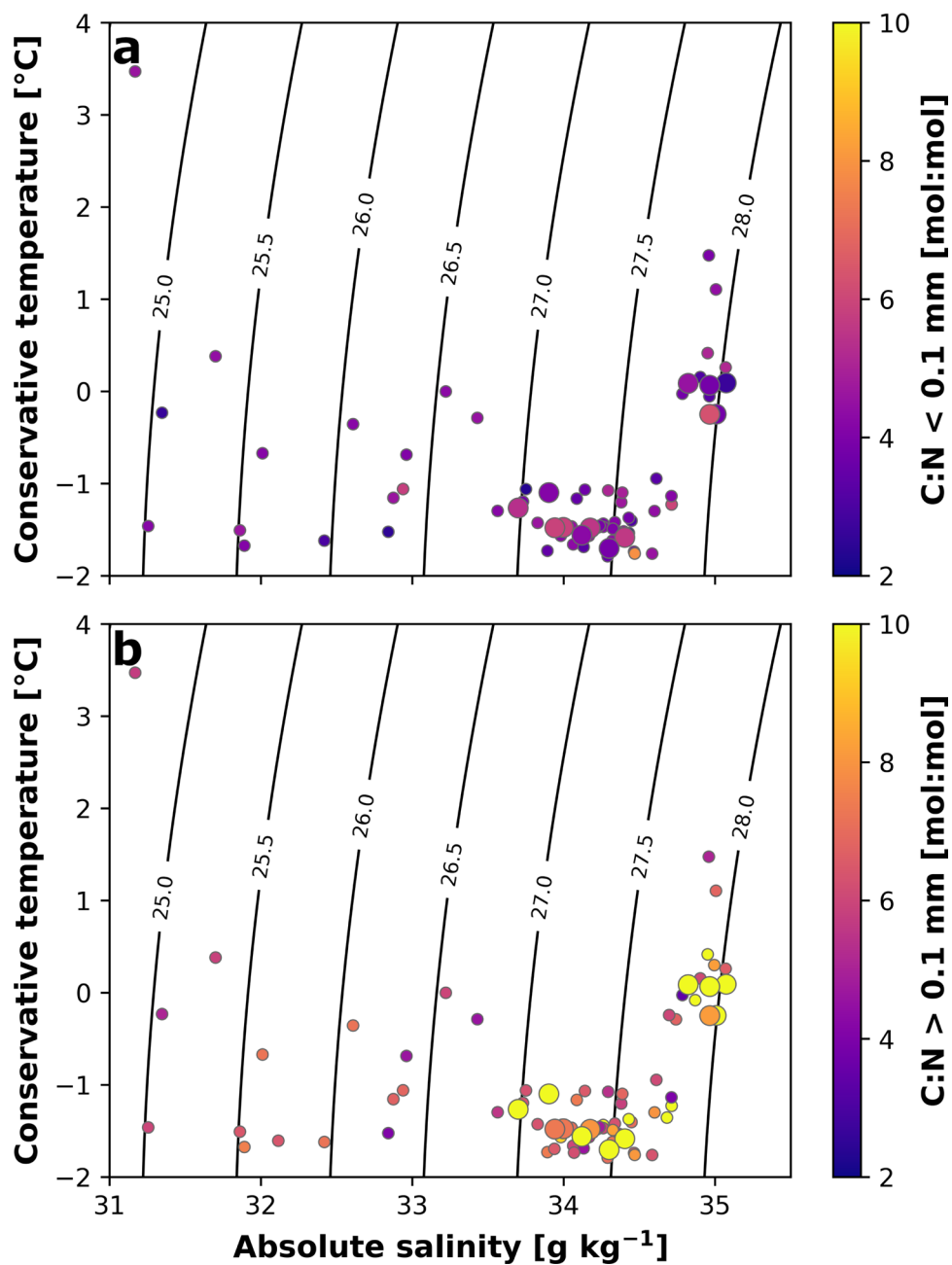
**Extended Data Fig. 4 | Molar carbon to nitrogen ratios in relation to conservative temperature and absolute salinity. a**, C:N ratios of the particle size fraction <0.1 mm. **b**, C:N ratios of the particle size fraction >0.1 mm. Isolines indicate potential density anomaly (σ₀) in kg m⁻³. Large dots represent measurements within the transect closest to the BSBW outflow north of Severnaya Zemlya.
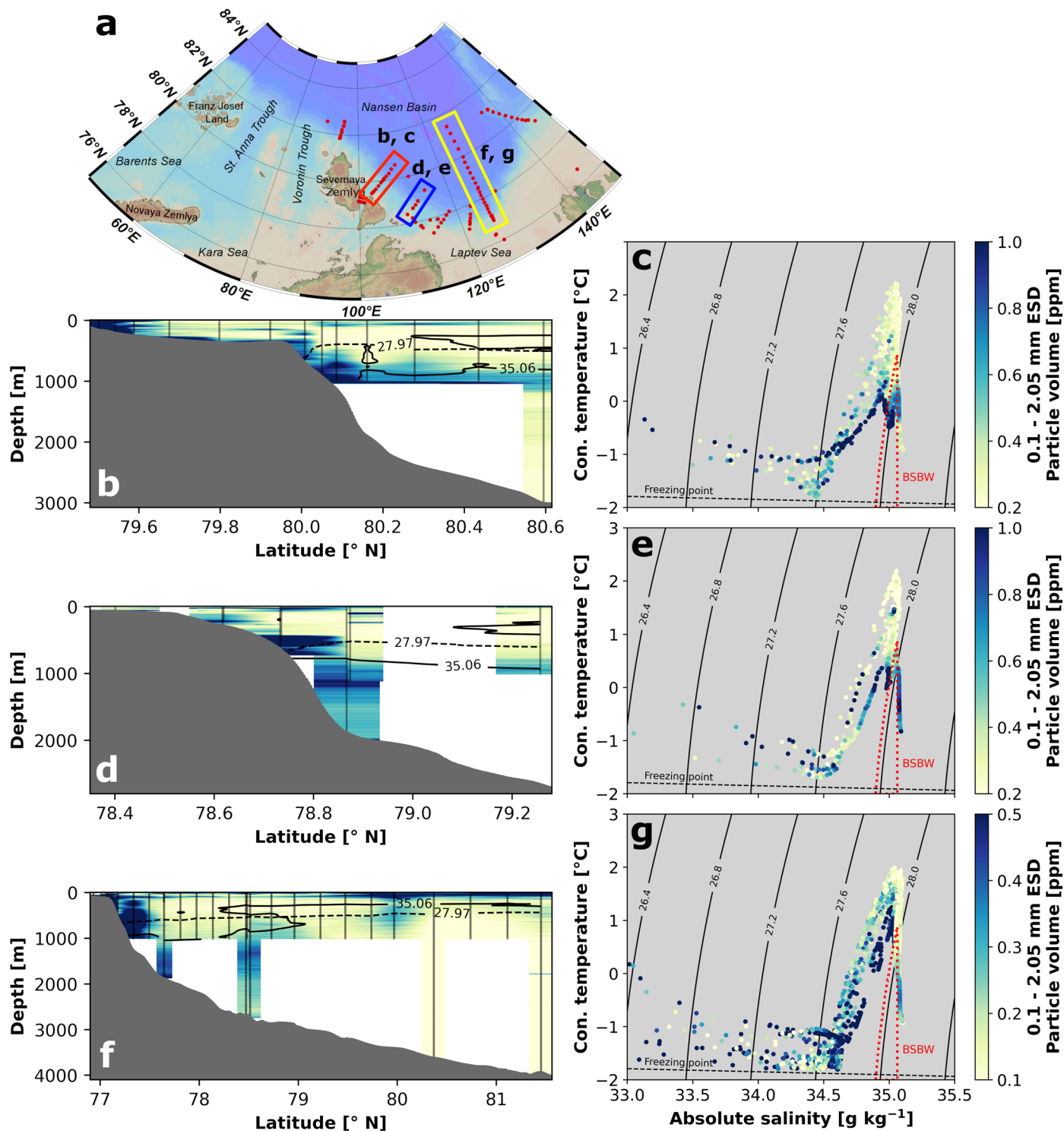
Extended Data Fig. 5 | Evolution of the deep particle plume and its relation to BSBW east of Severnaya Zemlya. a, Map of the research area including stations (red dots) and shown transects in rectangles. **b**, **d**, **f**, spatial particle volume distribution of the size fraction 0.1–2 mm ESD along the respective transect. The areas above the solid (absolute salinity <35.06 g kg⁻¹) and below the

dashed lines (potential density anomaly >27.97 kg m⁻³) indicate BSBW. **c**, **e**, and **g**, Conservative temperature and absolute salinity diagram with color-coded particle volume shows the relation of particle maxima with BSBW, marked by the red dashed water mass polygon. Isolines indicate potential density anomaly (σ_0) in kg m⁻³. Particle volumes have the same color bar in the respective transects.
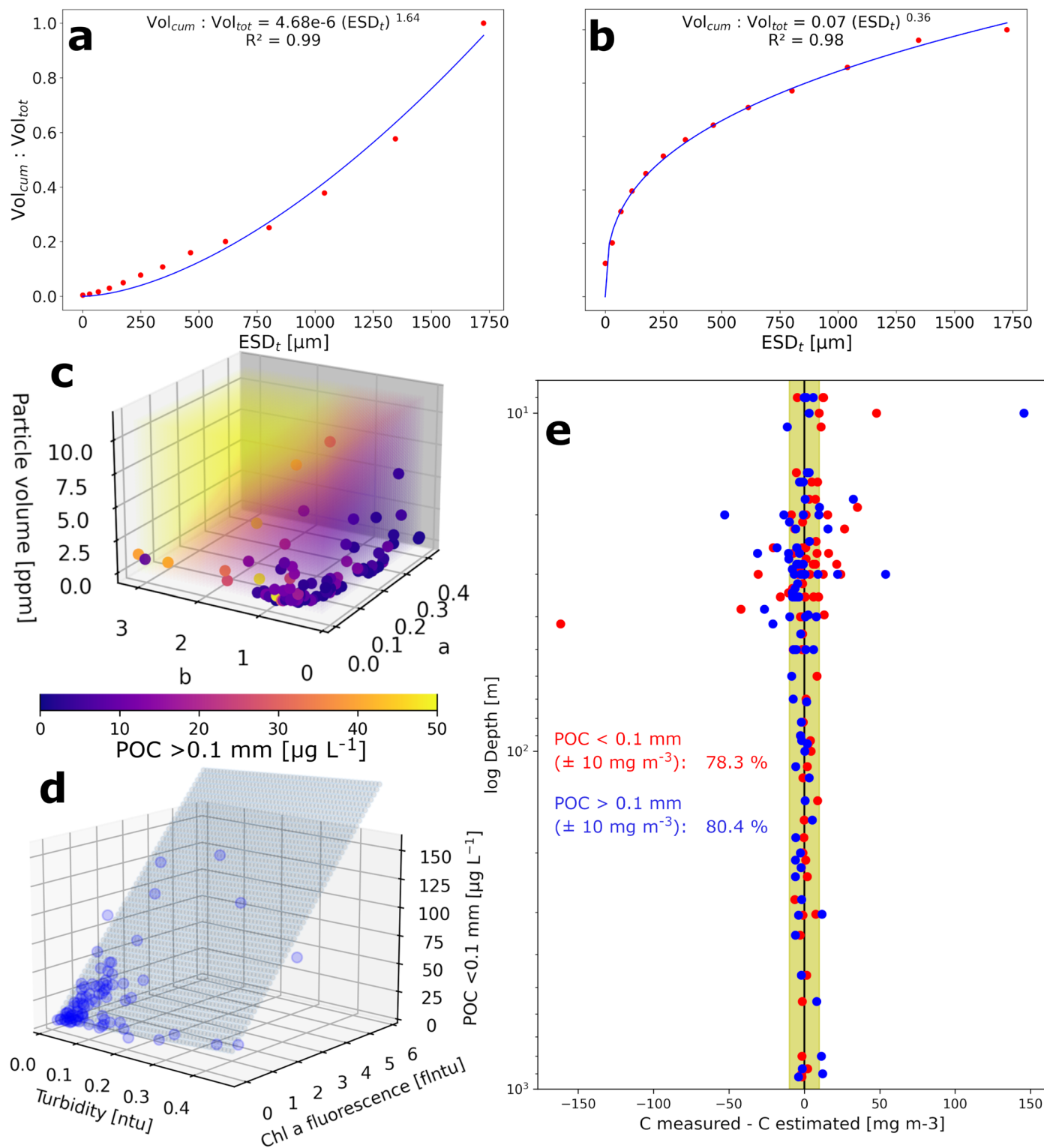
Extended Data Fig. 6 | Visualization of the sensor-based POC estimation.
a and **b**, examples for power law curve fitting on relative cumulative particle volume (cumulative volume: total volume; Vol_{cum}:Vol_{tot}) and transformed particle size bin centers (ESD_t) for one UVP depth bin of 5 m, respectively. **c**, regression for POC >0.1 mm between coefficients (a) and exponents (b) of the power law functions fitted over the relative cumulative particle size distributions, the particle volume between 0.1–2 mm, and the measured POC concentration >0.1 mm ESD. Color code represents 4th dimension for discrete measurements (dots) and the resulting regression (shade) of POC >0.1 mm. **d**, regression for POC< 0.1 mm between turbidity and chlorophyll a fluorescence and corresponding measurements of POC< 0.1 mm. Shaded area represents resulting regression for POC< 0.1 mm. **e**, Difference between measured concentrations from samples and estimated POC concentrations for the fraction <0.1 mm (red) and >0.1 mm (blue). Golden shade indicates area between −10 and 10 mg m^{-3}. See also Extended Data Table 2 for regression specifications and results.
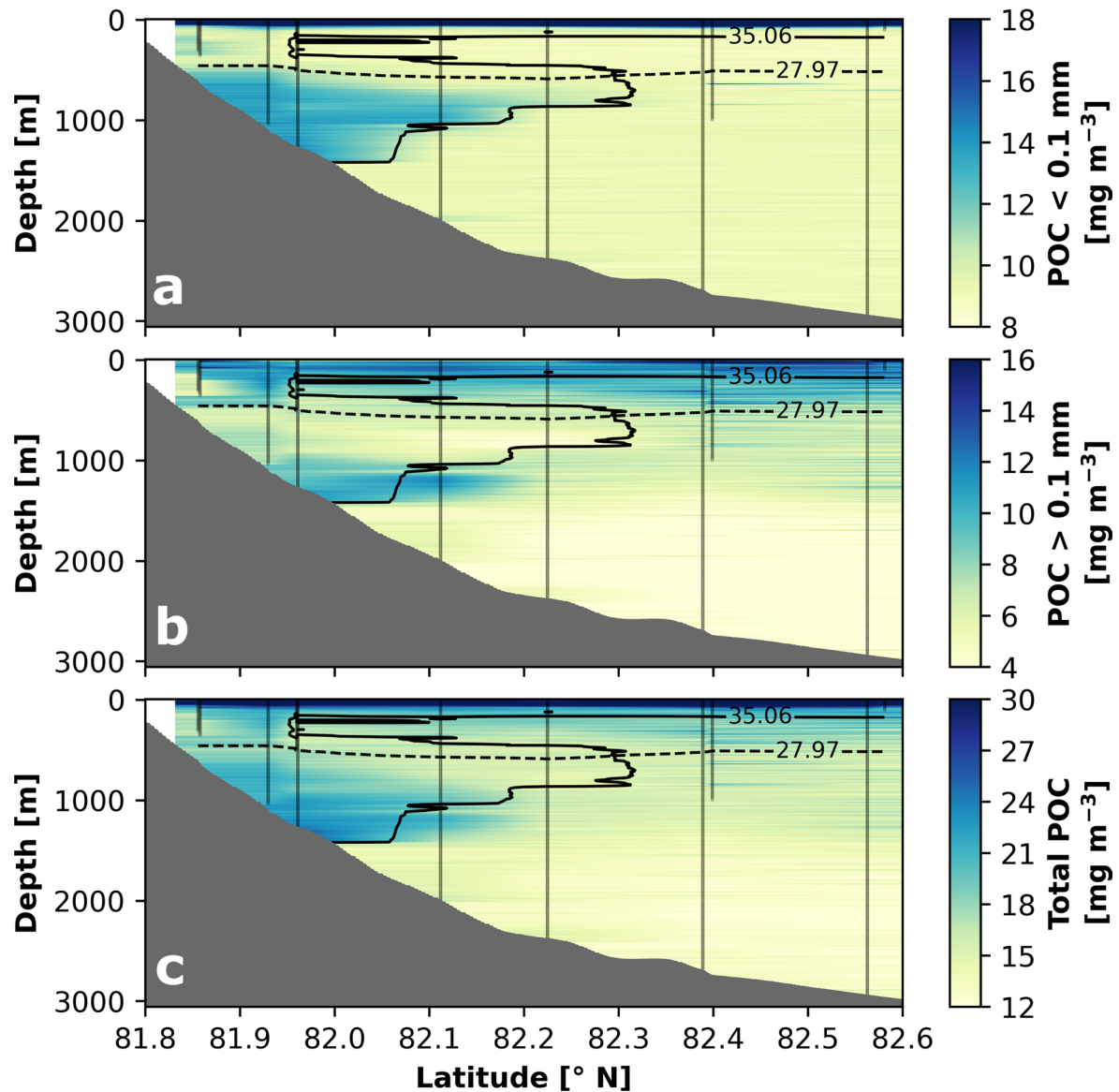
Extended Data Fig. 7 | Sensor-based estimates of the POC distribution north of Severnaya Zemlya. a, estimates of POC <0.1 mm based on reference measurements, turbidity and fluorescence sensor data. **b**, estimates of POC >0.1 mm based on reference measurements, as well as total particle volume and the particle size distribution from the UVP. **c**, Resulting summarized total POC distribution. The areas above the solid (absolute salinity <35.06 g kg⁻¹) and below the dashed isolines (potential density anomaly >27.97 kg m⁻³) indicate BSBW.
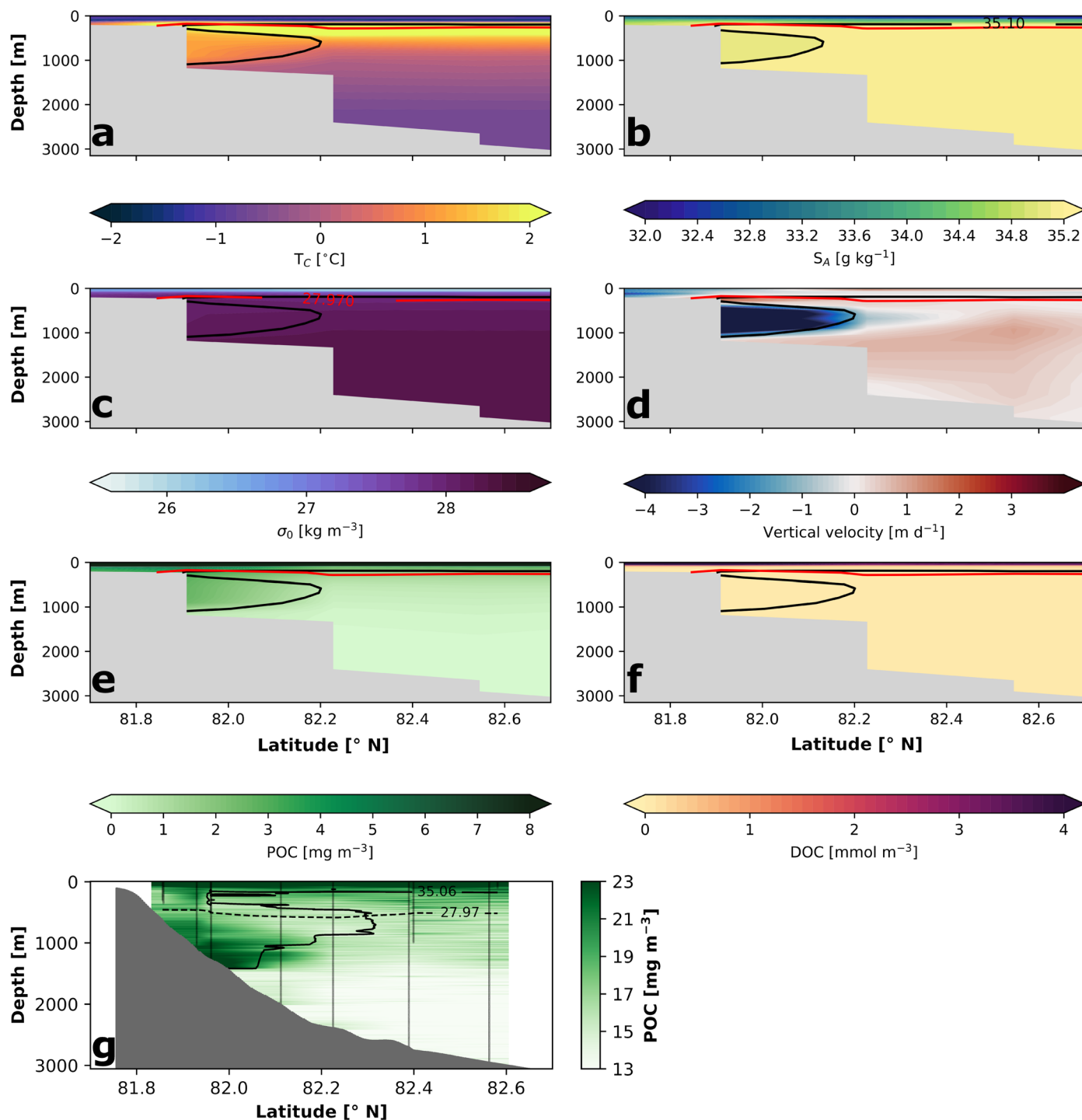
Extended Data Fig. 8 | Results of REcoM2 runs for the field transect North of Severnaya Zemlya and comparison with POC distribution in the field. REcoM outputs for August 2018 of: **a**, conservative temperature (°C), **b**, absolute salinity (g kg⁻¹), **c**, potential density anomaly (kg m⁻³), **d**, vertical velocity (m d⁻¹), **e**, particulate organic carbon (POC; mg m⁻³) and **f**, dissolved organic carbon (DOC; mmol m⁻³). **g**, field data estimates of the total POC concentration (mg m⁻³). Black isolines in **a-f** indicate absolute salinity of 34.94 g kg⁻¹ and red isolines potential density anomaly of 27.97 kg m⁻³ used for BSBW identification in the model. The area above the solid (absolute salinity <35.06 g kg⁻¹) and below the dashed isolines (potential density anomaly > 27.97 kg m⁻³) in **g** indicates BSBW as identified in the field.

Extended Data Table 1 | Results of FESOM 1.4 based particle backtracking of representative particle classes

Particle type	Sinking velocity [m d⁻¹]	Fraction of particles originating south of 81 °N [%]	Mean trajectory length of particles originating south of 81 °N [km]	Mean distance between release point and surface of particles originating south of 81°N [km]
Non-ballasted 0.08 mm ESD	1.03	50.2	5028	750
Non-ballasted 0.5 mm ESD	13.2	9.9	686	441
Ballasted 0.08 mm ESD	8.58	28.4	835	498

Extended Data Table 2 | Descriptions and results of regression models for estimation of POC concentrations smaller and larger than 0.1 mm

Regression model description for POC <0.1 mm

Dependent Variable	POC <0.1 mm [µg L^{-1}]
Regression model	Robust Linear Model
Weight function	Andrew's wave (tuning constant: 1.339)
Scaling for fitting	median absolute deviation
Link Function	identity
Optimization method	Iteratively reweighted least squares

Regression results for POC <0.1 mm

	Coefficient	Standard error	z	P > |z|
Intercept	9.1954	1.126	8.164	3.23e-16
Turbidity [ntu]	25.9341	9.321	2.782	5.39e-3
Chlorophyll a fluorescence [flntu]	32.1410	0.764	42.076	0.000

Regression model description for POC >0.1 mm

Dependent Variable	POC >0.1 mm [µg L^{-1}]
Regression model	Generalized Linear Model
Distribution Family	Gamma exponential
Link Function	logarithmic
Optimization method	Iteratively reweighted least squares

Regression results for POC >0.1 mm

Log-Likelihood	-292.61			
Deviance	82.685			
Pearson chi²	98.3			
	Coefficient	Standard error	z	P > |z|
Intercept	1.7350	0.263	6.603	4.03e-11
Particle size distribution coefficient a	-2.6996	1.216	-2.220	2.64e-2
Particle size distribution coefficient b	0.7251	0.248	2.924	3.45e-3
Total particle volume 0.1-2.05 mm [ppm]	0.1928	0.057	3.389	7.02e-4

Two-sided Z-tests used for significance tests were applied on non-adjusted (<0.1mm) or logarithmically adjusted data (>0.1mm).